Multi-modal Imaging of Retinal Oxygenation

BY

ANTHONY E. FELDER
B.S. Bioengineering, University of Illinois at Chicago, 2011

THESIS
Submitted as partial fulfillment of the requirements
for the degree of Doctor of Philosophy in Bioengineering
in the Graduate College of the
University of Illinois at Chicago, 2017

Chicago, Illinois

Defense Committee:
Dr. Mahnaz Shahidi, Ph.D., Chair and Advisor, Ophthalmology & Visual Sciences
Dr. Norman P. Blair, M.D., Ophthalmology & Visual Sciences
Dr. John R. Hetling, Ph.D., Bioengineering
Dr. Miiri A. Kotche, Ph.D., Bioengineering
Dr. Thomas J. Royston, Ph.D., Bioengineering

ACKNOWLEDGEMENTS

First and foremost, I would like to acknowledge my wife and parents, whose unwavering support has allowed me to pursue this degree. I would also like to thank Mahnaz, for extending the opportunity to work in her lab and for nurturing me as an academic and researcher. To Norman, your insight and critical feedback on our work has been invaluable and has resulted in some truly stimulating conversations. To the rest of my committee, thank you for your time and critical feedback. Last, and certainly not least, I would like to thank Marek, Tara, Mike, Ruth and Andrew – without your expertise and friendship, this work would have been impossible.

AEF

TABLE OF CONTENTS

LIST OF TABLES

LIST OF TABLES (continued)

LIST OF FIGURES

LIST OF FIGURES (continued)

LIST OF FIGURES (continued)

LIST OF FIGURES (continued)

LIST OF FIGURES (continued)

LIST OF FIGURES (continued)

LIST OF ABBREVIATIONS

1D	One-Dimensional
2D	Two-Dimensional
3D	Three-Dimensional
BF	Retinal Blood Flow
D	Retinal Vessel Diameter
D_A	Arterial D
D_AR	Ratio of D_A during DLFS to before DLFS
D_V	Venous D
D_VR	Ratio of D_V during DLFS to before DLFS
DLFS	Diffuse Light Flicker Stimulation
DO_2	Inner Retinal Oxygen Delivery
DR	Diabetic Retinopathy
F	Blood Flow
F_A	Arterial Blood Flow
F_V	Venous Blood Flow
FOV	Field of View
FOV_M	Maintained Field of View
FPS	Frames per Second
[Hgb]	Hemoglobin Concentration
k	Oxygen Solubility in Blood
MO_2	Inner Retinal Oxygen Metabolism
M_{tPO2}	Mean tPO_2
$[O_2]$	Oxygen concentration
$[O_{2A}]$	Arterial $[O_2]$
$[O_{2V}]$	Venous $[O_2]$
O_{2max}	Maximum Oxygen Carrying Capacity of Hemoglobin
OEF	Inner Retinal Oxygen Extraction Fraction
OEFR	Ratio of OEFR during DLFS to before DLFS
P_aO_2	Systemic Arterial PO_2
PLI	Phosphorescence Lifetime Imaging
ROI	Region of Interest
PO_2	Oxygen Tension
SD	Standard Deviation
SD_T	Total Mean Standard Deviation of Motion
SO_2	Retinal Vessel Oxygen Saturation of Hemoglobin
SO_{2A}	Arterial SO_2
$SO_{2A}R$	Ratio of SO_{2A} during DLFS to before DLFS
SO_{2V}	Venous SO_2
$SO_{2V}R$	Ratio of SO_{2V} during DLFS to before DLFS
SS	Sharpness Score
SV_{tPO2}	Spatial Variation of tPO_2
tPO_2	Retinal Tissue PO_2
V	Retinal Volume

SUMMARY

The retina is a light-sensitive tissue located at the back of the eye and plays a key role in vision. To maintain visual function, the amount of oxygen in the retina (retinal oxygenation) is highly regulated under normal physiological conditions. However, alteration of retinal oxygenation is implicated in common vision-threatening retinal diseases including diabetic retinopathy, glaucoma and macular degeneration. Additionally, retinal oxygenation can be perturbed and characterized by the physiological challenge of diffuse light flicker stimulation (DLFS). Therefore, research that characterizes retinal oxygenation and its response to DLFS in health and disease is essential. To date, available techniques for the direct assessment of retinal oxygenation are invasive and cannot be used in humans. Therefore, markers of retinal oxygenation in humans – retinal vessel diameter (D), retinal vessel oxygen saturation of hemoglobin (SO_2) and the inner retinal oxygen extraction fraction (OEF) – are measured non-invasively instead. However, in animals, retinal oxygenation may be directly assessed by measurement of retinal tissue oxygen tension (tPO_2). This thesis describes novel techniques to assess retinal oxygenation markers in humans and tPO_2 in rats.

An optical imaging system for the non-invasive measurement of retinal oxygenation markers in humans was developed and then applied to assess the effects of diabetic retinopathy disease stage and DLFS on markers. Additionally, the system was modified to measure and mathematically model the temporal dynamic responses of retinal oxygenation markers to DLFS. To address limitations in subjects' fixation during the assessment of these temporal dynamics, a system for real-time image stabilization was developed. Finally, a technique for the three-dimensional assessment of retinal tPO_2 in rats was developed, permitting the evaluation and assessment of multifocal retinal oxygenation abnormalities.

I. INTRODUCTION

The retina is one of the most metabolically active tissues in the human body,[1, 2] requiring a constant supply of oxygen to meet the high energy demands of vision. Indeed, the amount of oxygen in the retina (retinal oxygenation) has been implicated in common vision-threatening diseases, including diabetic retinopathy,[3-5] macular degeneration[6] and glaucoma.[7] Therefore, techniques that assess retinal oxygenation are necessary to understand retinal physiology in health and disease.

Retinal oxygenation in humans cannot be directly assessed by current techniques, which are either invasive or require injection of agents that are not approved for human use by the U.S. Food and Drug Administration.[8-10] Therefore, retinal oxygenation in humans is assessed using non-invasively measured markers of oxygenation. These markers include retinal vessel diameter (D) and oxygen saturation of hemoglobin (SO_2). Retinal vessel D has been measured using systems such as conventional fundus imaging[11] and the retinal vessel analyzer.[12, 13] Retinal vessel SO_2 is commonly measured by dual-wavelength retinal spectrophotometry,[14-17] although recent research has also demonstrated measurement by photoacoustic ophthalmoscopy[18] and visible optical coherence tomography.[19]

Previous studies have characterized retinal oxygenation during diffuse light flicker stimulation (DLFS). DLFS is a physiological challenge to the retina that has been shown to stimulate neural activity,[20] dilate retinal vessels,[21-24] increase blood flow,[24-26] and alter SO_2 in retinal veins.[23, 24] However, D, SO_2 and their DLFS-induced responses represent characteristics of the retinal vessels alone and cannot provide direct information on the retinal tissue.

Previous studies in cerebral tissues[27] and the rat retina[28] have quantified a tissue oxygenation marker called oxygen extraction fraction (OEF). OEF in the inner retina represents

the fraction of oxygen extracted from the retinal vasculature by the retinal tissue, and under steady state conditions, quantifies the ratio of inner retinal oxygen metabolism to oxygen delivery. Thus, OEF can provide information on the ability of a tissue's oxygen delivery to address its metabolic demand. However, neither OEF nor its DLFS-induced responses have been reported in human retina under health or disease.

Therefore, we developed a novel optical imaging system for simultaneous assessment of retinal oxygenation markers (D, SO_2 and OEF) before and during DLFS, providing insight into retinal physiology and how the retina accommodates challenges like DLFS.[16] We then used the optical imaging system to assess both the effects of diabetic retinopathy (DR) disease stage and DLFS on retinal oxygenation markers, elucidating retinal pathophysiology at stages of DR.[29] These two studies provided information on the effect of DLFS after a fixed duration, but could not describe the temporal dynamics of retinal oxygenation markers during DLFS. Thus, we modified the image acquisition protocol of the optical imaging system to assess the temporal dynamic responses of retinal oxygenation markers to DLFS, permitting the modeling of these dynamic responses. This modeling revealed the time-course of changes in retinal oxygenation markers during DLFS, further elucidating retinal physiology. However, the assessment of these temporal dynamics required longer image acquisition times, during which subjects may lose fixation. Therefore, an additional novel optical imaging system was developed for real-time image stabilization, which prevented the loss of imaging data due to poor subject fixation.[30]

In contrast to studies in humans, retinal oxygenation can be directly assessed in animals by measuring retinal tissue oxygen tension (tPO_2). Current methods to measure tPO_2 include oxygen-sensitive microelectrodes[31-34] and phosphorescence lifetime imaging (PLI).[35, 36] The oxygen-sensitive microelectrode technique is considered the most accurate due to its direct

sampling, high sensitivity and depth discrimination, but it is highly invasive and can only provide measurement of tPO_2 through the retinal depth at single point locations. In contrast, PLI has been adapted to measure tPO_2 through the retinal depth at vertically contiguous regions,[37] partially overcoming the limited spatial assessment of tPO_2 by oxygen-sensitive microelectrodes. However, neither of these techniques can measure volumetric retinal tPO_2.

Therefore, we developed a novel technique for the three-dimensional (3D) measurement of tPO_2 in rats. The technologies from our previous studies for two-dimensional retinal tissue PLI[37] and 3D retinal vascular PLI[9] were combined here to acquire depth-resolved measurement of tPO_2 at multiple vertical and horizontal contiguous locations across the retina. Thus, retinal tPO_2 volumes were generated, permitting the quantitative 3D assessment of retinal oxygenation under health and disease.

II. BACKGROUND

The Retina

The human eye is a complex organ that is responsible for vision. As indicated in Figure 2.1A, the major tissues of the eye include the cornea, iris, lens, retina and optic nerve. Both the cornea and lens are transparent tissues which refract light, limited by the opening in the iris, to a focus on the retina. The retina is neural tissue located within the posterior inner surface of the eye and consists of eight layers and two membranes, as shown in Figure 2.1B. Considering the eye as a sphere, the retina is commonly discussed as two halves – the inner and outer retina – corresponding to the portions of the retina which are closest to the sphere's center (inner) and farthest from the sphere's center (outer). Thus, the inner retina spans roughly from the inner limiting membrane to the inner nuclear layer and the outer retina spans from the outer plexiform layer to the pigment epithelium.[38]

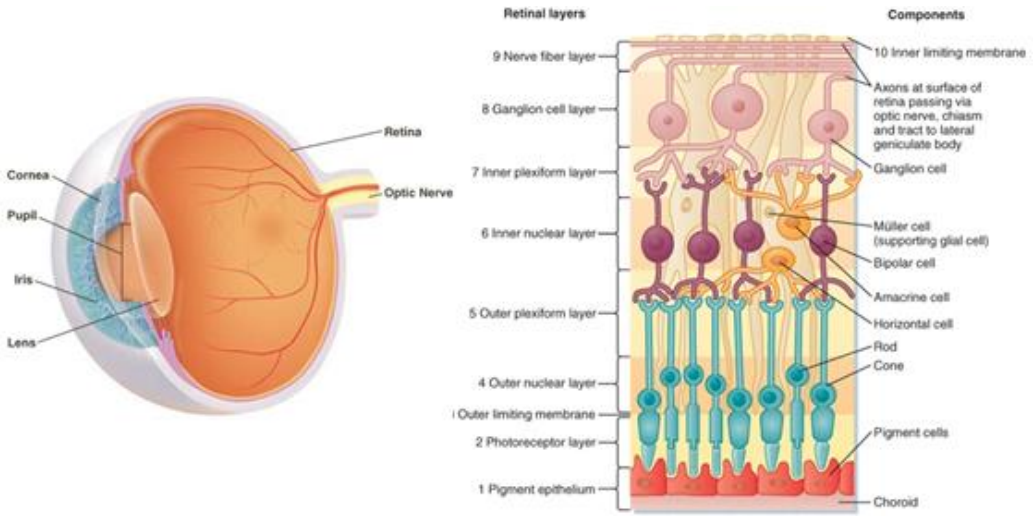

Figure 2.1 (Left) A sagittal plane cross-section schematic of the human eye with major tissues labeled. Adapted from Northwestern Medicine (encyclopedia.nm.org). (Right) Labeled retinal layers from the inner retina (top) to the outer retina (bottom). Adapted from Berne and Levy, Physiology.[39]

The primary function of the retina is to detect light and convert it to electrical signals. As light enters the eye, it passes through the inner retina to the outer retina, where phototransduction occurs in the photoreceptors. Phototransduction in the human eye is the process of converting visible light photons into electrical signals by rhodopsin-mediated intra-cellular biochemical cascades.[40] These signals are transmitted and integrated through the interconnecting and ganglion neurons via action potentials and are eventually delivered to the cerebral cortex via the optic nerve for further visual processing.[41]

Retinal Oxygenation

The retina is one of the most metabolically active tissues in the human body[1, 2] To address the retinal metabolic activity, oxygen is continuously delivered to the retina by two distinct vascular beds: the retinal vasculature and the choroidal vasculature.[38] The retinal vasculature is located within, and primarily supplies oxygen to, the inner retina, whereas the choroidal vasculature is located immediately external to the retina and primarily supplies oxygen to the outer retina. The retinal metabolic consumption of oxygen in conjunction with the oxygen delivery from the two vascular beds generates a characteristic distribution of oxygen through the retinal depth.[31, 32, 42] Physiological and pathological events may affect the retinal metabolic activity and/or the ability of either vascular bed to deliver oxygen, which in turn affects retinal oxygenation. Therefore, it is imperative to measure retinal oxygenation to elucidate the mechanisms of visual function in both health and disease.

Retinal Blood Flow and Oxygen Transport

As a first approximation, the retina may be modeled as a mass of tissue with a single artery and vein. By the conservation equation, we write that,

$$\frac{d}{dt}massO_2 = \frac{d}{dt}mass_{enter} - \frac{d}{dt}mass_{exit} + \frac{d}{dt}mass_{gen} - \frac{d}{dt}mass_{con} \quad 2.1$$

where $massO_2$ is the amount of oxygen in the retina, $mass_{enter}$ is the amount of oxygen entering the retina, $mass_{exit}$ is the mass of oxygen exiting the retina, $mass_{gen}$ is the amount of oxygen generated in the retina and $mass_{con}$ is the amount of oxygen consumed by the retina.

We first make four assumptions: 1) oxygen enters the retina from the artery only; 2) oxygen leaves the retina from the vein only; 3) no oxygen is generated within the retina; 4) oxygen is consumed solely by metabolic activity. Expanding Equation 2.1 yields,

$$\frac{d}{dt}massO_2 = \frac{d}{dt}massO_{2A} - \frac{d}{dt}massO_{2V} - \frac{d}{dt}massO_{2met} \quad 2.2$$

where $massO_{2A}$ is the mass of oxygen in the artery and $massO_{2met}$ is the mass of oxygen used for retinal energy metabolism. We now make several substitutions to facilitate further mathematics. In general, $\frac{d}{dt}mass$ can be expressed as the product of flow (F; vol/time) and concentration ([]; mass/vol). Similarly, mass may be expressed as the product of volume (V) and concentration. Here, we also define the rate that oxygen is consumed by retinal energy metabolic activity as *oxygen metabolism* (i.e., $\frac{d}{dt}massO_{2met} = MO_2$ in units of mass O_2/time) and the rate that oxygen is delivered to the retina by the artery (A) as *oxygen delivery* (i.e., $\frac{d}{dt}massO_{2A} = F_A * [O_{2A}] = DO_2$; mass/time). Thus, we write

$$V\frac{d}{dt}[O_2] = DO_2 - F_V[O_{2V}] - MO_2 \quad 2.3$$

where $[O_2]$ is the concentration of oxygen in the retina, $[O_{2V}]$ is the concentration of oxygen in the vein and F_V is venous blood flow. However, since the retinal vascular system is an end-artery system, retinal blood flow is conserved between arteries and veins and is henceforth denoted as BF.

$$V\frac{d}{dt}[O_2] = DO_2 - BF[O_{2V}] - MO_2 \tag{2.4}$$

Now we make one last assumption, 5) the retina is well-mixed, such that the concentration of oxygen in the retina is similar to that of the nearby vein. Expanding Equation 2.4 according to the fifth assumption yields,

$$V\frac{d}{dt}[O_2] = DO_2 - BF[O_2] - MO_2 \tag{2.5}$$

Thus, the conservation equation has been expanded to a linear, ordinary differential equation. It should be noted here that for empirical mathematical evaluation, we also assume BF (and thus MO_2 and DO_2) is time-invariant. While this holds for the steady-state approximation, this equation does not hold faithfully represent unsteady-state conditions. Regardless, the differential equation in 2.5 is solved in the next several equations.

$$V\int \frac{d[O_2]}{DO_2 - BF[O_2] - MO_2} = \int dt \tag{2.6}$$

$$V\frac{ln(DO_2 - BF[O_2] - MO_2)}{-BF} = t + C \tag{2.7}$$

$$DO_2 - BF[O_2] - MO_2 = Ce^{-\frac{BF}{V}t} \tag{2.8}$$

$$[O_2] = \frac{1}{BF}\left(DO_2 - MO_2 - Ce^{-\frac{BF}{V}t}\right) \tag{2.9}$$

Using the initial condition, t=0, $[O_2]$ is equal to some initial concentration ($[O_{2o}]$), the integration constant is given as

$$C = DO_2 - MO_2 - BF[O_{2o}] \quad 2.10$$

Substituting this constant into the original equation yields $[O_2]$ as a function of time, V, BF, DO_2, MO_2, and $[O_{2o}]$.

$$[O_2] = \frac{1}{BF}\left[DO_2 - MO_2 - (DO_2 - MO_2 - BF[O_{2o}])e^{-\frac{BF}{V}t}\right] \quad 2.11$$

This relationship may be rearranged to solve for MO_2.

$$MO_2 = \frac{DO_2\left(1 - e^{-\frac{BF}{V}t}\right) - BF[O_2] + BF[O_{2o}]e^{-\frac{BF}{V}t}}{1 - e^{-\frac{BF}{V}t}} \quad 2.12$$

This is an equation for MO_2 in the non-steady state, assuming that V, BF and DO_2 (containing $[O_{2A}]$) are time-invariant. However, it's commonly of interest to evaluate at steady state conditions (i.e., $t \rightarrow \infty$):

$$MO_2 = DO_2 - BF[O_2] \quad 2.13$$

Recall assumption 5 (well-mixed model) and the definition of DO_2, allowing us to express MO_2 using arterial and venous oxygen concentrations:

$$MO_2 = BF([O_{2A}] - [O_{2V}]) \quad 2.14$$

This is a derivation of Fick's 1st Law which states that flux is equal to the negative product of the diffusion coefficient and the first derivative of solute concentration.[43] Thus, in our simplified model, MO_2 can be calculated as the product of retinal blood flow and the arteriovenous oxygen concentration difference.

Markers of Retinal Oxygenation

As discussed in the introduction, retinal oxygenation is most directly assessed using oxygen-sensitive microelectrodes or PLI to measure retinal tPO_2. However, these techniques are

highly invasive or rely on the injection of oxygen-sensitive molecules, rendering them unsuitable for human study. Therefore, retinal oxygenation in humans is assessed by vascular and tissue markers of retinal oxygenation. Vascular markers include D and SO_2, and tissue markers include OEF.

OEF represents the ability of a tissue to extract oxygen from its blood supply to satisfy metabolic activity. Under steady state conditions, OEF quantifies the ratio of MO_2 to DO_2 and has been assessed in the human brain[27, 44, 45] and rat retina.[28, 46]

$$OEF = \frac{MO_2}{DO_2} \tag{2.15}$$

It is worth noting that we assume all oxygen extracted from the vasculature is ultimately metabolized. However, realistically, some oxygen may be lost to the vitreous[47] through diffusion and thus the MO_2 term may slightly overestimate actual metabolized oxygen.

We expand MO_2 and DO_2 according to the mathematics from the previous section to yield,

$$OEF = \frac{MO_2}{DO_2} = \frac{BF[O_{2A}]\left(1 - e^{-\frac{BF}{V}t}\right) - BF[O_{2V}] + BF[O_{2o}]e^{-\frac{BF}{V}t}}{BF[O_{2A}]\left(1 - e^{-\frac{BF}{V}t}\right)} \tag{2.16}$$

Recall, that this relationship given by the ratio of MO_2 to DO_2 only applies to steady state conditions (namely, $t \to \infty$), thus,

$$OEF = \frac{MO_2}{DO_2} = \frac{[O_{2A}] - [O_{2V}]}{[O_{2A}]} \tag{2.17}$$

Here, the arterial and venous oxygen concentration terms account for both hemoglobin-bound and hemoglobin-unbound oxygen that is present in the blood. In general, $[O_2]$ terms may be expressed as,

$$[O_2] = O_{2max} * [Hgb] * SO_2 + k * PO_2 \quad (2.18)$$

where O_{2max} is the maximum oxygen carrying capacity of hemoglobin, [Hgb] is the measured hemoglobin concentration, SO_2 is the oxygen saturation in percent, and k is the oxygen solubility in blood. Since k is small (0.003 $mLO_2\,dL^{-1}mmHg^{-1}$),[48] oxygen content is closely approximated by the hemoglobin-bound oxygen alone. Equation 2.17 is rewritten as

$$OEF = \frac{MO_2}{DO_2} = \frac{(O_{2max} * [Hgb] * SO_{2A}) - (O_{2max} * [Hgb] * SO_{2V})}{(O_{2max} * [Hgb] * SO_{2A})} \quad (2.19)$$

where SO_{2A} and SO_{2V} are the arterial and venous oxygen saturations, respectively. Simplifying, we write the final expression for calculation of OEF.

$$OEF = \frac{MO_2}{DO_2} = \frac{SO_{2A} - SO_{2V}}{SO_{2A}} \quad (2.20)$$

Thus, under steady state, OEF can be calculated by SO_{2A} and SO_{2V} alone, without direct measurement of retinal BF and used to provide information on the ratio of MO_2 to DO_2.[16, 28] This relationship is valid for any tissue with the simplified modeling as provided in the previous section and may be applied to the inner retina. As described before, the retinal vasculature primarily provides oxygen to the inner retina. Thus, measuring SO_{2A} and SO_{2V} from the retinal vasculature can provide information on the ratio of inner retinal MO_2 and DO_2. In this thesis, SO_{2A} and SO_{2V} are concerning the retinal vasculature and OEF, MO_2 and DO_2 are concerning the inner retina tissue.

Oximetry

Oximetry is a method to assess the oxygen saturation of hemoglobin in blood and was developed from spectrophotometry – the non-invasive study of chemical-based absorptivity. This technique utilizes the difference in absorption spectra between oxygenated hemoglobin and

de-oxygenated hemoglobin to determine the relative saturation of blood. Figure 2.2 indicates the absorption spectra for human adult hemoglobin.

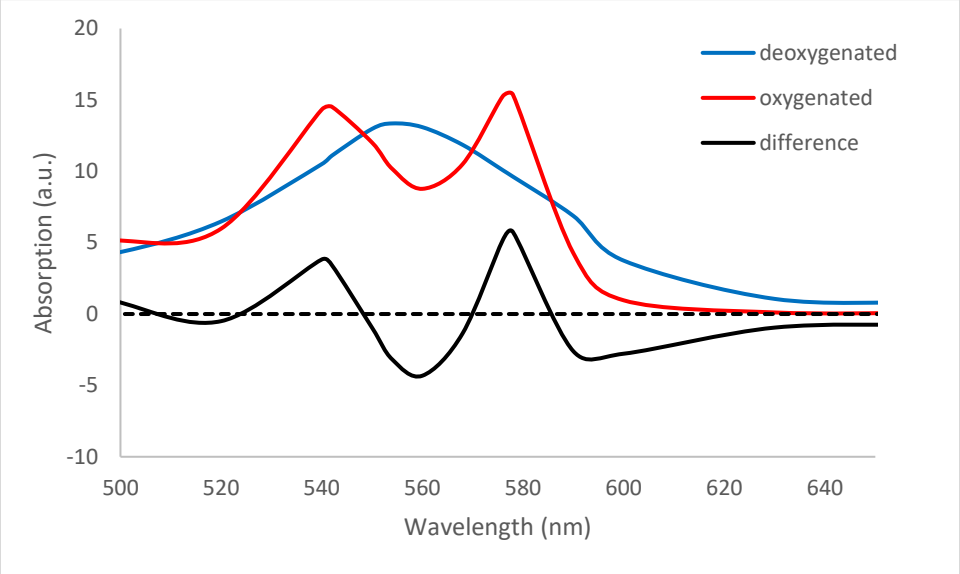

Figure 2.2 Absorption spectrum of deoxygenated hemoglobin, oxygenated hemoglobin, and the difference between the two (oxy-deoxy) in adult humans. Intersection between the difference curve and dashed line (0-absorption reference) indicates wavelengths where oxygenated and deoxygenated absorption are equal (isosbestic wavelengths). All data adapted from Zijlstra et al.[49]

Retinal oximetry is commonly performed by acquiring retinal reflectance images using two wavelengths, one that is "insensitive" to oxygenation (i.e., at an isosbestic point, a wavelength where absorptivity does not change between deoxygenated and oxygenated hemoglobin) and one that is "sensitive" to oxygenation (a wavelength where absorptivity changes between deoxygenated and oxygenated hemoglobin).[17] An optical density (OD) is calculated for each vessel at both wavelengths.[15] This calculation normalizes the retinal vessel to the immediate surrounding tissue in an effort to account for other absorbing tissues present in the retina. The ratio of these OD measurements (ODR) is then calculated to normalize vessel reflectance to the isosbestic wavelength. Since ODR is linearly related to SO_2, a specific empirical calibration is then derived for the imaging system and wavelengths.[11, 50, 51] It is

important to note that wavelengths must be carefully selected; if neither wavelength is isosbestic, the calibration from ODR to SO_2 becomes nonlinear, complicating calibration.[17] Regardless, oximetry is a technique for non-invasive measurement of SO2 in vasculature.

Phosphorescence Lifetime Imaging

Phosphorescence lifetime imaging (PLI) is an optical imaging technique to measure oxygen tension (PO_2). This technique utilizes an oxygen-sensitive molecule (oxyphor) whose phosphorescence is variably quenched depending on the surrounding oxygen concentrations. Thus, increasing oxygen concentrations results in shorter phosphorescence lifetimes (i.e., more rapid decay of the phosphorescence).[52] Phosphorescence lifetime can be measured in two ways:[8] 1) in the temporal domain, or 2) in the frequency domain. In the temporal domain, the oxyphor is excited by a light impulse and the exponential decay in phosphorescence is measured over some finite time (microseconds).[53, 54] In the frequency domain, both the excitation light and camera intensifier are modulated temporally to produce sinusoidally-varying excitation light relative to the camera sensor. This excitation light then produces phosphorescence emission at the same modulation frequency, but at some phase delay relative to the excitation light, which is related to the phosphorescence lifetime.[8, 35] Regardless of which approach is used, the phosphorescence lifetime is then related to PO_2 using the Stern-Volmer equation,[55]

$$PO_2 = \frac{1}{K_Q}\left(\frac{1}{\tau} - \frac{1}{\tau_0}\right) \qquad 2.23$$

where K_Q is the quenching constant of the oxyphor ($mmHg^{-1}\mu s^{-1}$), τ is the phosphorescence lifetime (μs) and τ_0 is the lifetime in a zero-oxygen environment.

PO_2 can be calculated wherever the oxyphor can be delivered and imaged in the presence of oxygen. Multiple previous studies have measured retinal vascular PO_2 using an albumin-bound pd-porphyrin molecule (oxyphor R0).[35, 56-58] Additionally, it is also possible to measure PO_2 in extra-vascular tissues, using another oxyphor that is not albumin-bound (oxyphor R2).[59] For example, this oxyphor has been injected intravitreally and used to image retinal tPO_2.[37]

III. A METHOD FOR SIMULTANEOUS ASSESSMENT OF RETINAL OXYGENATION MARKERS IN RESPONSE TO DIFFUSE LIGHT FLICKER STIMULATION IN HUMANS

(Parts of) this chapter was (were) previously published as: Anthony E. Felder, Justin Wanek, Norman P. Blair, Mahnaz Shahidi; Inner Retinal Oxygen Extraction Fraction in Response to Light Flicker Stimulation in Humans. Invest. Ophthalmol. Vis. Sci. 2015;56(11):6633-6637.

Introduction

Retinal oxygenation is highly regulated to ensure visual function. Therefore, assessment of retinal oxygenation is vital to understanding retinal function in health and disease. In humans, vascular markers of retinal oxygenation – retinal vessel diameter (D), retinal vessel oxygen saturation of hemoglobin (SO_2) – are commonly measured non-invasively.[14, 21, 60-62] In addition to measuring D and SO_2 at baseline conditions (i.e., steady-state), previous studies have also characterized the functional response of these markers to the physiological challenge of diffuse light flicker stimulation (DLFS). The effect of DLFS on retinal vascular oxygenation markers can provide information on how the retinal vasculature accommodates physiological challenges in health and disease. DLFS has been shown to increase neural activity, augmenting D,[22] retinal blood flow (BF)[25] and SO_{2V}.[23] However, vascular markers cannot directly provide information on the retinal tissue and the state of its oxygenation.

Recently, OEF has been introduced as a novel tissue marker of retinal oxygenation,[27, 28] but OEF has not been previously reported in human retina. OEF can provide knowledge of how retinal oxygenation is regulated in health and disease and, at steady state conditions, quantifies

the ratio of inner retinal oxygen metabolism (MO_2) to oxygen delivery (DO_2) without measuring BF.[28] Moreover, the effect of DLFS on OEF has not been reported in humans and can provide information on the ability of the retinal circulation to address changes in the metabolic demand of the retinal tissue.

In the current chapter, a novel optical imaging system for simultaneous measurement of retinal oxygenation markers (D, SO_2 and OEF) before and during DLFS in humans is demonstrated. We tested the hypothesis that OEF remains unchanged during DLFS, indicating that DLFS-induced changes in MO_2 are met in equal magnitude by changes in DO_2 in healthy human subjects.

Materials and Methods

Subjects

The research study was approved by an Institutional Review Board at the University of Illinois at Chicago. Prior to enrollment, the research study was explained to the subjects and informed consents were obtained according to the tenets of the Declaration of Helsinki. A total of 20 healthy subjects (age: 53 ± 17 years; 11 male, 9 female) participated in the study. Exclusion criteria were abnormal retinal examination, history of eye disease or refractive error > 6 diopters. Subjects' pupils were dilated using 1% tropicamide and 2.5% phenylephrine. Subjects were seated in front of the modified slit lamp biomicroscope with their heads resting on a chin and forehead support. A light emitting diode was presented to the fellow eye as a fixation target. Subjects were continuously light adapted during imaging. Imaging was performed in one eye of each subject. In four subjects, three sets of repeated images were acquired before DLFS to determine the reproducibility of measurements.

Instrumentation

A novel optical imaging system was developed to coordinate measurement of D, SO_2 and OEF with DLFS (Figure 3.1). A slit lamp biomicroscope (Zeiss, Jena, Germany) was modified to accommodate a rapid-switching filter wheel (Thorlabs, Newton, New Jersey) and triggered light block. The filter wheel contained three bandpass filters to provide retinal illumination using light at 606 ± 5 nm, 570 ± 5 nm and 530 ± 5 nm wavelengths (Edmund Optics, Barrington, New Jersey). Light at 606 and 570 nm wavelengths was used to acquire retinal reflectance images at oxygen-sensitive and oxygen-insensitive wavelengths,[49] respectively. Light at 530nm was used during image alignment and DLFS to elicit a maximal vasodilatory response.[21, 63] DLFS was provided by modulating 530 nm wavelength at 10 Hz with 50% duty cycle. All images were acquired using an electron multiplying charge coupled device camera (QImaging, Surrey, British Columbia). A customized control software was developed in LabView (National Instruments, Austin, TX, USA) and incorporated an Arduino microprocessor (Arduino, Ivrea, Italy) to coordinate filter wheel rotation, DLFS and image acquisition.

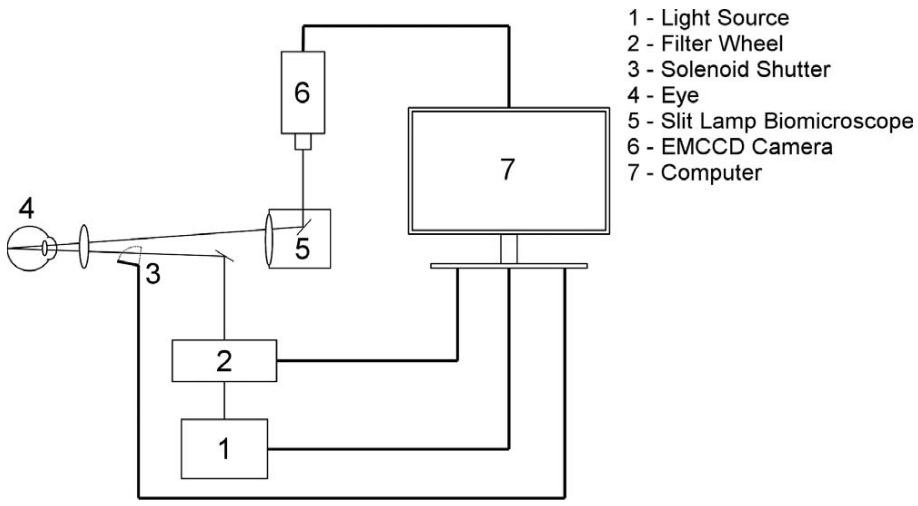

Figure 3.1 Schematic of the novel optical imaging system for simultaneous assessment of retinal vessel diameter, oxygen saturation of hemoglobin and inner retinal oxygen extraction fraction before and during diffuse light flicker stimulation. Thick lines indicate hardware connection and thin lines indicate the optical beam path.

Imaging Protocol

Subjects were seated at the modified slit lamp and image alignment was performed for less than two minutes using light at 530nm (45 µW) while room lights were turned off. Before DLFS, nine retinal reflectance images were acquired at 606 nm (230 µW) and 570 nm (180 µW) within three seconds. DLFS was then provided for 60 seconds using 530 nm light (25 µW). At the end of 60 seconds, retinal reflectance images were again acquired at 606 and 570 nm during continuous flicker using roughly 50% of the light power compared to before DLFS.

Image Analysis

Images from before and during DLFS were visually inspected to remove those containing low contrast, blinking, or large subject motion. Remaining images were registered using ImageJ (National Institutes of Health, Bethesda, MD, USA) and then averaged to generate a mean image at 606 and 570 nm wavelengths ($image_{606}$ and $image_{570}$, respectively) before and during DLFS.

Mean images were then manually registered. Our previously reported customized software for retinal vessel image analysis[64] was modified for use here. A circumpapillary region of interest (ROI) which extended from one to two disc diameters from the perimeter of the optic disc, was selected. Retinal vessels within the ROI were segmented using a Hessian-based Frangi "vesselness" filter[65] and a centerline was generated for each using a Euclidian distance transformation. Perpendicular intensity profiles (PIP) from both mean images were generated every seven pixels along the centerlines.

Retinal D was measured using the full-width half maximum of PIPs from $image_{570}$, according to the method a previous study.[66] Measurements of D were superimposed on the $image_{570}$ and gross boundary errors were manually eliminated after visual inspection (Figure 3.2 Left). Measurements of D were averaged per vessel and again per vessel type to yield an average arterial and venous D (D_A and D_V, respectively) for each subject. D_A and D_V in units of micrometers were calculated using a constant calibration factor of 6.63 μm/px, which was derived based on previously published optic disk size in healthy human subjects.[67]

For each vessel within the ROI, optical densities (OD) were calculated using PIPs at both mean images. OD was calculated as $\log (I_{outside}/I_{inside})$, where $I_{outside}$ and I_{inside} are the average pixel intensity values outside and inside the vessel along a PIP, respectively.[15] Here, I_{inside} was measured using the lowest 50% of intensity values to help minimize the effect of specular reflection.[11] $I_{outside}$ was measured using a percentage of background pixels located at the minima of the PIP second order derivative.[66] Optical density ratios were calculated as OD_{606}/OD_{570}, where OD_{606} and OD_{570} were the OD measurements from $image_{660}$ and $image_{570}$, respectively.[15] There is a known artificial relationship between optical density ratio and vessel diameter, which was corrected using the calibration methodology from a previous study.[11] Corrected optical

density ratio values were converted to SO_2 by linear regression[11, 17] using previously published SO_2 values in healthy human subjects (Figure 3.2 Right).[68] Measurements of SO_2 were averaged per vessel and again per vessel type to yield an average arterial and venous SO_2 (SO_{2A} and SO_{2V}, respectively) for each subject.

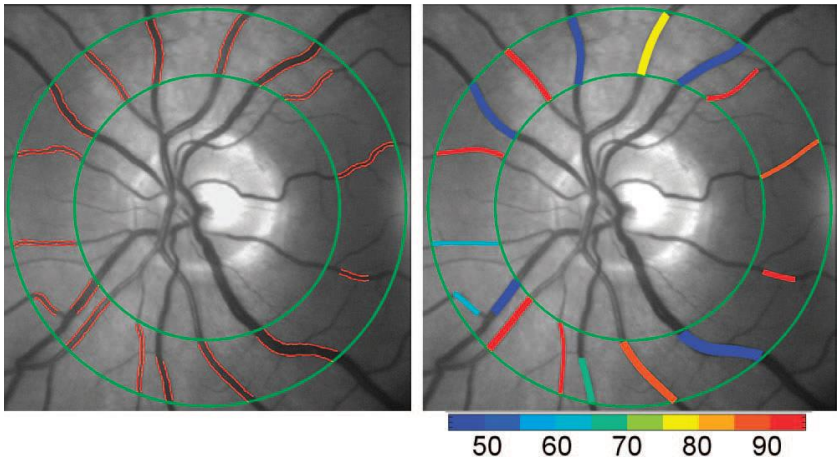

Figure 3.2 Example of a retinal reflectance image acquired in a healthy human subject using 570 nm light. Vessel boundaries within the circumpapillary region of interest (green circles) are indicated in red (Left). Mean oxygen saturation of hemoglobin (measured in percentage) for each vessel within the circumpapillary region of interest is overlaid on the retinal image in pseudocolor (Right).

Oxygen Extraction Fraction

As outlined in the background section, under steady state conditions, inner retinal OEF quantifies the ratio of inner retinal oxygen metabolism (MO_2) to inner retinal oxygen delivery (DO_2) and was calculated as $((SO_{2A}-SO_{2V})/SO_{2A})$, independent of BF.

The Effect of DLFS

To study the effect of DLFS on markers (D_A, D_V, SO_{2A}, SO_{2V} and OEF), the fractional changes in markers were assessed as the ratio of the metric value during DLFS to before DLFS. Marker ratios were denoted by the inclusion of an 'R' to the metric name. For example, the

DLFS-induced change in D_A (D_AR) was calculated as $D_{A\_during\_DLFS}/D_{A\_before\_DLFS}$. Marker ratios ($D_AR$, D_VR, $SO_{2A}R$, $SO_{2V}R$ and OEFR) were calculated for each subject.

Data Analysis

Reproducibility of measurements was determined by coefficient of variation and intraclass correlation coefficients from three repeated measurements before DLFS in four subjects. A mean and standard deviation (SD) of marker values before and during DLFS were calculated. Similarly, a mean and SD of marker ratios were calculated. The effect of DLFS was determined by paired t-test. Statistical significance was accepted at $P \leq 0.05$.

Results

Coefficients of variation and intraclass correlation coefficients for marker values before DLFS (N = 4) are summarized in Table 3.1.

TABLE 3.1 COEFFICIENT OF VARIATION AND INTRACLASS CORRELATION COEFFICIENT OF REPEATED RETINAL OXYGENATION MARKER MEASUREMENTS BEFORE DIFFUSE LIGHT FLICKER STIMULATION

Marker	Coefficient of Variation (%)	Intraclass Correlation Coefficient
D_A (μm)	2.1	0.85
D_V (μm)	1.3	0.99
SO_{2A} (%)	1.6	0.96
SO_{2V} (%)	3.9	0.93
OEF	4.9	0.83

Marker values before and during DLFS are summarized in Table 3.2. As expected, D_V was larger than D_A and SO_{2A} was greater than SO_{2V}. D_A and D_V significantly increased with DLFS ($P < 0.001$) by an average of 7 and 6%, respectively. SO_{2A} did not significantly change

with DLFS (P = 0.5) whereas SO_{2V} significantly increased (P = 0.004) by an average of 10%. Correspondingly, OEF significantly decreased (P = 0.001) by an average of 14%.

TABLE 3.2 EFFECTS OF DIFFUSE LIGHT FLICKER STIMULATION (DLFS) ON RETINAL OXYGENATION MARKERS IN HEALTHY HUMAN SUBJECTS

Marker	Before DLFS	During DLFS	P-Value	Marker Ratio
D_A (μm)	84 ± 7	90 ± 8	< 0.001	1.07 ± 0.05
D_V (μm)	109 ± 17	115 ± 16	< 0.001	1.06 ± 0.04
SO_{2A} (%)	92 ± 6	92 ± 6	0.5	0.99 ± 0.04
SO_{2V} (%)	58 ± 10	53 ± 9	0.004	1.10 ± 0.16
OEF	0.37 ± 0.08	0.31 ± 0.07	0.001	0.86 ± 0.19

Discussion

In the current chapter, inner retinal OEF was determined before and during DLFS in human subjects for the first time, using a custom designed optical imaging system. OEF decreased with DLFS, indicating the DLFS-induced change in DO_2 exceeded that of MO_2, thus our hypothesis was rejected.

Values of retinal oxygenation markers were repeatable to within 5%. As expected, D_V was significantly larger than D_A, and SO_{2A} was significantly greater than SO_{2V}. Both D_A and D_V significantly dilated with DLFS, in agreement with previous studies.[23, 25, 69-71] Furthermore, SO_{2A} did not significantly change with DLFS, while SO_{2V} significantly increased, consistent with the findings of a previous study.[23] Therefore, our optical imaging system was able to detect the physiological perturbations caused by DLFS.

In the current study, mean OEF before DLFS was 0.37, indicating that 37% of oxygen available from the retinal circulation was extracted for inner retinal oxygen metabolism. This value is comparable to those from previous studies in human brain (0.44)[27] and rat inner retina (0.46).[28] Mean OEF during DLFS was 0.31, resulting in an OEFR less than unity. This result

indicates the DLFS-induced change in DO_2 exceeded that of MO_2. The change in DO_2 likely occurs due to an increase in BF during functional hyperemia as supported by our finding of vasodilation. Although the exact vaso-regulatory mechanisms[72-74] involved in functional hyperemia remain to be elucidated, they result in unequal alterations in DO_2 and MO_2. This may be necessary to raise venous capillary PO_2 in order to drive oxygen to regions of the retina which are farther away from the blood vessels.

Recently, efforts have been made to directly quantify MO_2 in humans using combined measurements of SO_2 and BF.[75] Although, DLFS has been shown to increase MO_2 in animals,[76, 77] its effect on MO_2 in humans had not been reported at the time of this study. From the results in the current chapter, namely OEFR, we cannot provide absolute measurement of the DLFS-induced changes in MO_2 or DO_2. However, using our results in addition to that of a previous study, it is possible to estimate these changes. Thus, we rewrite Equation 2.20 to express OEFR using MO_2R and DO_2R. DO_2R can then be expressed as the product of BFR and $SO_{2A}R$. Hence, MO_2R is given by:

$$MO_2R = OEFR * DO_2R = OEFR * BFR * SO_{2A}R \quad 3.1$$

Using our values of mean OEFR (0.86) and $SO_{2A}R$ (0.99), and the value of BFR (1.59) measured in retinal vasculature by Garhofer et al,[25] we can estimate both MO_2R and DO_2R. Thus, we reason that MO_2 would increase by 35% (MO_2R = 1.35) and DO_2 would increase by 57% (DO_2R = 1.57) during DLFS. Indeed, shortly after the publication of this work, a study by Palkovits et al[24] directly measured a MO_2R of 1.35 and a DO_2R of 1.56 in humans, consistent with our estimations. Thus, a decrease in OEF during DLFS corresponds to an DLFS-induced increase in MO_2 and even greater increase in DO_2.

While inner retinal OEF was used to quantify the ratio of MO_2 to DO_2 based on oxygen saturation measurements in the retinal circulation, it inherently does not account for the potential contribution of oxygen supply from the choroidal circulation. Hence, measurements of OEFR may have been influenced by DLFS-induced changes in the relative proportion of the retinal mass supplied by the retinal and choroidal circulations. This relative proportion is determined by oxygen gradients through the retinal depth, which depend on oxygen consumption rates of the inner and outer retina, inner retinal oxygen delivery, and choroidal oxygen delivery. Therefore, without empirical data on intraretinal oxygen tension profiles during DLFS, the effects of dual circulatory beds on OEFR measurements remain to be elucidated.

There were several limitations to this work. First, as with all optical imaging techniques, image quality may affect measurements. However, the reproducibility of measurements was sufficient for detection of changes due to DLFS. Second, mean light levels before and during DLFS were not matched. A reduction in the mean light level during the 1-minute duration of DLFS may have induced a small change in the photoreceptor oxygen consumption. However, this change is primarily addressed by the choroidal circulation. Therefore, the reduction in mean light levels between image alignment and DLFS is expected to minimally influence measurements of OEFR which predominately reflects the retinal circulation and inner retinal neural activity. Third, the effects of pigmentation on measurements of SO_2[11] and optical properties on measurements of D were not addressed. However, since DLFS-induced changes were evaluated within subjects and the statistical significance of the differences was high, these factors likely contributed minimally to the results. Fourth, absolute measurements of MO_2 and DO_2 were not possible since BF was not measured, but their ratio was derived based on measurements of OEF. Consequently, the findings based on OEFR measurements cannot

directly address the adequacy of DLFS-induced compensatory changes in BF in response to tissue need.

In summary, a novel optical imaging system was developed for the simultaneous measurement of retinal oxygenation markers before and during DLFS. As indicated by the measured decrease in OEF, the DLFS-induced change in DO_2 exceeded that of MO_2 in healthy human subjects.

IV. THE EFFECTS OF DIABETIC RETINOPATHY STAGE AND DIFFUSE LIGHT FLICKER STIMULATION ON RETINAL OXYGENATION MARKERS

(Parts of) this chapter was (were) previously published as: Anthony E. Felder, Justin Wanek, Norman P. Blair, Charlotte E. Joslin, Katherine C. Brewer, Felix Y. Chau, Jennifer I. Lim, Yannek I. Leiderman, Mahnaz Shahidi; The Effects of Diabetic Retinopathy Stage and Light Flicker on Inner Retinal Oxygen Extraction Fraction. Invest. Ophthalmol. Vis. Sci. 2016;57(13):5586-5592.

Introduction

Diabetic retinopathy (DR) is a progressive vascular disorder and the leading cause of vision loss in working-age adults.[78, 79] Thus, the study of DR and its effect on retinal oxygenation markers is of critical importance. Previous studies have reported that DR significantly affects retinal vessel diameter (D)[80, 81] and oxygen saturation of hemoglobin (SO_2).[4, 5] Moreover, studies have demonstrated that changes in D are related to the incidence[82, 83] and progression of DR.[80] In addition to changes in D and SO_2 at baseline, previous studies have evaluated the effect of diffuse light flicker stimulation (DLFS) on these markers in DR. DR has been shown to significantly reduce the DLFS-induced responses in D[84-86] and SO_2[3] compared to healthy subjects.

However, neither the inner retinal oxygen extraction fraction (OEF) nor its DLFS-induced changes have been reported at stages of DR. OEF at stages of DR can provide information on how DR affects inner retinal oxygen metabolism (MO_2) relative to inner retinal

oxygen delivery (DO_2). Furthermore, measurements of D and SO_2 as well as their responses to DLFS in DR are typically not assessed simultaneously, potentially affecting results due to inter-test variability. Simultaneous assessment of retinal oxygen markers (D, SO_2, and OEF) and their responses to DLFS at stages of DR may be useful to elucidate the pathophysiology of DR. Therefore, in the current chapter, we tested the hypothesis that retinal oxygenation markers and their responses to DLFS are altered at stages of DR.

Materials and Methods

Subjects

The research study was approved by an Institutional Review Board at the University of Illinois at Chicago. Prior to enrollment, the research study was explained to the subjects and informed consents were obtained according to the tenets of the Declaration of Helsinki. A total of 130 subjects participated in the study. Subjects were classified by clinical retinal examination as normal control without diabetes (NC; N = 42) or diabetic without retinopathy (NDR; N = 32), with non-proliferative retinopathy (NPDR; N = 42) or proliferative retinopathy (PDR; N = 14). Due to the aggressive nature of the disease, all PDR subjects had received panretinal photocoagulation (PRP) treatment prior to imaging. Exclusion criteria included history of stroke or myocardial infarction within 3 months prior to imaging, active angina, sickle cell disease, glaucoma, age-related macular degeneration, retinal vascular occlusion, refractive error > 6 diopter, or intraocular surgery within 6 months prior to imaging.

Subjects' pupils were dilated using 1% tropicamide and 2.5% phenylephrine and subjects were seated in front of the modified slit lamp biomicroscope with their heads resting on a chin and forehead support. A light emitting diode was presented to the fellow eye as a fixation target.

Subjects were continuously light adapted during imaging. Imaging was performed in one eye of each subject, based on exclusion criteria.

Instrumentation

The optical imaging system for simultaneous measurement of retinal oxygenation markers before and during DLFS as described in Chapter 3 was used here.[16] Briefly, a rapid switching filter wheel was fitted with three bandpass filters and incorporated into a slit lamp biomocrscope to provide retinal illumination at 570, 606 and 530 nm wavelengths. Light at 570 and 606 was used for oximetry, serving as the oxygen-insensitive and oxygen-sensitive wavelengths, respectively. DLFS was provided by attenuating light at 530 nm at 10 Hz with 50% duty cycle for 60 seconds. Images from 606 and 570 nm wavelengths were registered using an automated algorithm and averaged to generate a single mean image at each wavelength. A circumpapillary region of interest extending between one and two disc radii from the perimeter of the optic disc was selected. Measurements of D and SO_2 from each vessel within this circumpapillary region of interest were averaged to yield a mean D_A, D_V, SO_{2A} and SO_{2V}. These mean values were determined for each subject before and during DLFS stimulation. Inner retinal OEF was calculated as $((SO_{2A}-SO_{2V})/SO_{2A})$. As described in Chapter 3, DLFS-induced retinal oxygenation marker ratios (D_AR, D_VR, $SO_{2A}R$, $SO_{2V}R$ and OEFR) were calculated by dividing the value of the marker during DLFS by the value before DLFS.

Data Analysis

The distributions of markers were evaluated to assess data normalcy and identify outliers.[87] Regression diagnostics including Cook's distance were performed to assess the linear

relationship between DR stage and each metric to identify data points that were outliers, had leverage, or were influential. Three outliers were identified, which were removed from further analyses. Subsequent testing for each metric indicated normalcy. The effect of DLFS on measurements of markers within each DR stage group (an intragroup comparison) was performed by paired t-test using marker values before and during DLFS. Descriptive statistics were compared for demographic variables using the χ^2 test and t-tests. The independent effects of DR stage group (an intergroup comparison) on measurements of markers before DLFS and marker ratios were assessed using linear regression analysis. Multivariable linear regression[88] models were constructed using *a priori*–selected covariates (age, race, sex, eye examined) from univariate models to compute the parameter estimates and 95% confidence intervals. All statistical tests were two-sided and significance was accepted at $P \leq 0.05$. All statistical analyses were performed using SAS version 9.4 (SAS Institute, Inc., Cary, NC, USA).

Results

Demographic data for subjects are presented in Table 4.1. The distribution of races differed significantly among DR stage groups ($P < 0.001$). Mean ages were not significantly different among DR stage groups ($P = 0.2$).

TABLE 4.1 CHARACTERISTICS OF SUBJECTS STRATIFIED BY DIABETIC RETINOPATHY (DR) STAGE GROUP

		Total (N = 130)	**NC (N = 42)**	**NDR (N = 32)**	**NPDR (N = 42)**	**PDR (N = 14)**	**P-value[a]**
Sex	Male	48	14	10	19	5	0.59
	Female	82	28	22	23	9	
Race	African American	51	5	21	19	6	< 0.001
	White	50	33	5	9	3	
	Hispanic	29	4	6	14	5	
Age (years)	<30	2	1	0	0	1	0.33
	30-39	9	2	3	3	1	
	40-49	22	7	6	5	4	
	50-59	38	10	9	15	4	
	60-69	43	12	10	17	4	
	≥70	16	10	4	2	0	
Eye	OD	86	29	22	25	10	0.74
	OS	44	13	10	17	4	

[a]P-values derived using chi-square test of proportions

Unadjusted means of markers before DLFS, during DLFS and the marker ratios stratified by DR stage group are presented in Table 4.2.

TABLE 4.2 UNADJUSTED RETINAL OXYGENATION MARKERS (MEAN ± SD) BEFORE, DURING DIFFUSE LIGHT FLICKER STIMULATION (DLFS) AND THEIR DLFS-INDUCED MARKER RATIOS STRATIFIED BY DIABETIC RETINOPATHY (DR) STAGE GROUP

Marker	**Flicker Condition**	**DR Stage Group**			
		NC	**NDR**	**NPDR**	**PDR**
D_A (μm)	Before DLFS	86 ± 8	90 ± 12	92 ± 11	82 ± 11
	During DLFS	91 ± 7**	94 ± 12**	96 ± 12**	86 ± 12**
	D_AR	1.07 ± 0.05	1.04 ± 0.04	1.05 ± 0.06	1.05 ± 0.05
D_V (μm)	Before DLFS	106 ± 15	107 ± 15	110 ± 15	105 ± 11
	During DLFS	112 ± 15**	112 ± 15**	115 ± 15**	110 ± 10**
	D_VR	1.06 ± 0.04	1.05 ± 0.03	1.04 ± 0.05	1.05 ± 0.04
SO_{2A} (%)	Before DLFS	92 ± 6	96 ± 5	98 ± 7	108 ± 8
	During DLFS	92 ± 5	95 ± 6	97 ± 7	107 ± 7
	$SO_{2A}R$	1.00 ± 0.04	0.99 ± 0.04	0.99 ± 0.04	0.99 ± 0.03
SO_{2V} (%)	Before DLFS	60 ± 9	61 ± 7	66 ± 7	66 ± 7
	During DLFS	64 ± 7**	65 ± 5**	67 ± 8*	70 ± 6**
	$SO_{2V}R$	1.09 ± 0.14	1.07 ± 0.11	1.02 ± 0.08	1.06 ± 0.06
OEF	Before DLFS	0.36 ± 0.08	0.36 ± 0.07	0.33 ± 0.07	0.38 ± 0.09
	During DLFS	0.30 ± 0.06**	0.32 ± 0.05**	0.31 ± 0.07**	0.34 ± 0.08**
	OEFR	0.87 ± 0.15	0.89 ± 0.12	0.96 ± 0.15	0.89 ± 0.08

*P-values < 0.1; p-values derived using paired t-tests
**P-values ≤ 0.05; p-values derived using paired t-tests

Unadjusted D, SO_2 and OEF before and during DLFS are shown in Figures 4.1, 4.2 and 4.3, respectively.

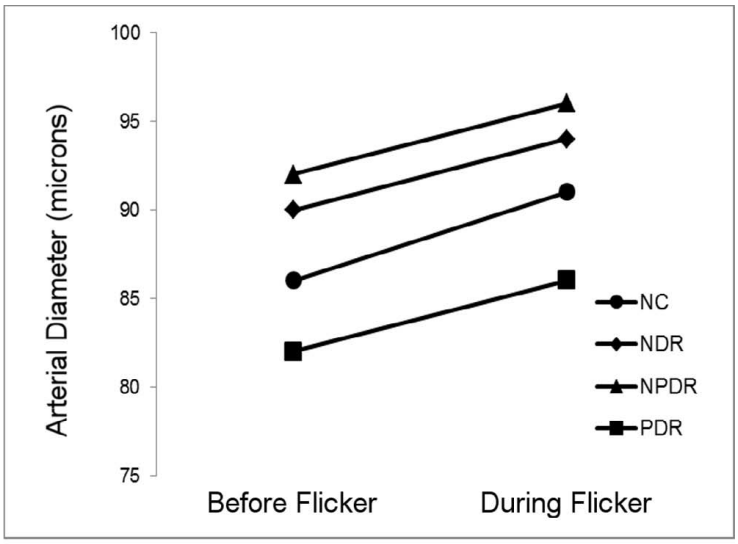

A

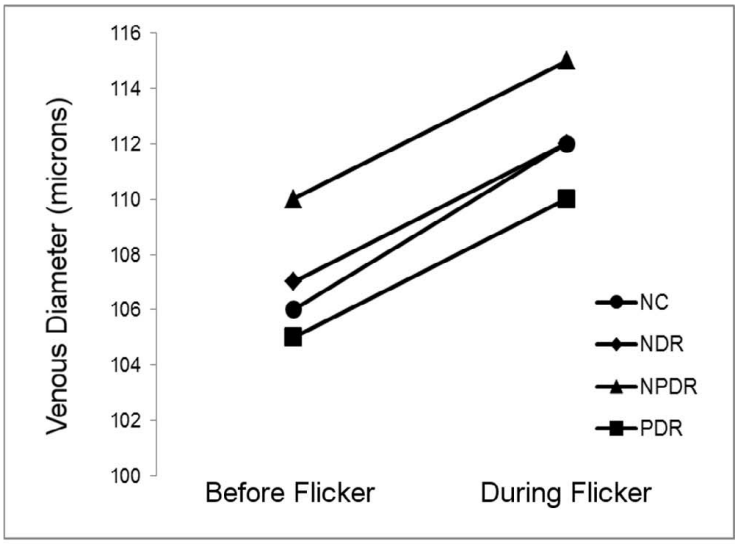

B

Figure 4.1 Mean retinal arterial (A) and venous (B) diameter measurements before and during diffuse light flicker stimulation in each diabetic retinopathy stage group.

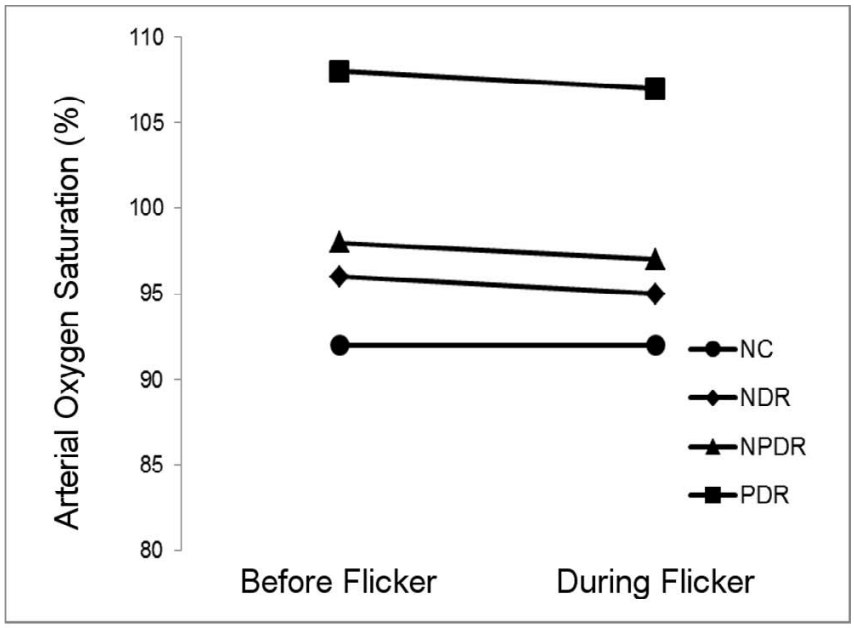

A

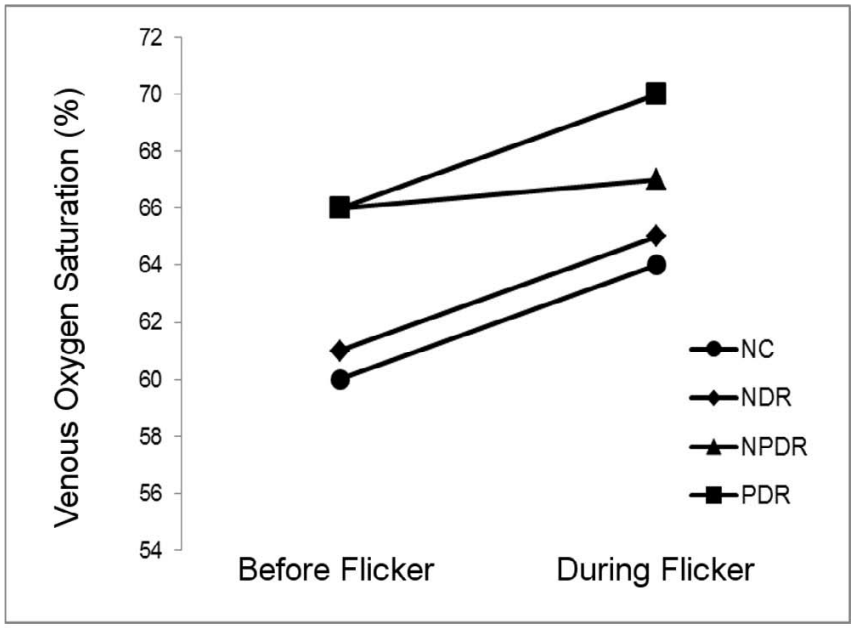

B

Figure 4.2 Mean retinal arterial (A) and venous (B) oxygen saturation of hemoglobin before and during diffuse light flicker stimulation in each diabetic retinopathy stage group.

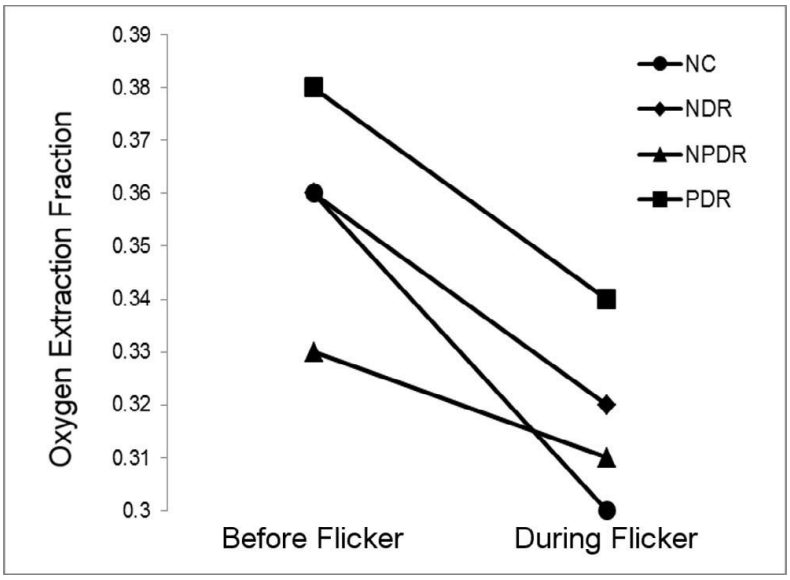

Figure 4.3 Mean inner retinal oxygen extraction fraction before and during diffuse light flicker stimulation in each diabetic retinopathy stage group.

For the adjusted model, means of markers and marker ratios were statistically adjusted to adjust for covariates (age, race, sex, eye examined).

Effect of DR Stage: Intergroup Comparison

Differences in estimated means of markers before DLFS between DR stage groups are provided in Table 4.3. D_A was larger in NPDR compared to both NC and NPDR subjects ($P \leq 0.01$). Additionally, D_A was larger in NDR compared to PDR subjects ($P = 0.02$). D_V did not differ among DR stage groups ($P \geq 0.16$). SO_{2A} was higher in all DR stage groups compared to NC subjects ($P \leq 0.02$) and was higher in PDR compared to NDR and NPDR subjects ($P < 0.001$). SO_{2V} was higher in NPDR and PDR compared to NC ($P \leq 0.01$) and NDR subjects ($P \leq 0.02$). OEF was lower in NPDR compared to NDR and PDR subjects ($P \leq 0.002$). OEF tended to be lower in NPDR compared to NC subjects ($P = 0.07$).

TABLE 4.3 DIFFERENCES IN ESTIMATED MEANS OF RETINAL OXYGENATION MARKERS BEFORE DIFFUSE LIGHT FLICKER STIMULATION BETWEEN EACH DIABETIC RETINOPATHY (DR) STAGE GROUP AND A REFERENCE GROUP

Marker	Reference	DR Stage Group		
		NDR	NPDR	PDR
D_A (μm)	NC	NS	5.4**	NS
	NDR		NS	-7.0**
	NPDR			-9.2**
D_V (μm)	NC	NS	NS	NS
	NDR		NS	NS
	NPDR			NS
SO_{2A} (%)	NC	3.5**	5.6**	16.3**
	NDR		NS	12.8**
	NPDR			10.7**
SO_{2V} (%)	NC	NS	6.1**	6.9**
	NDR		5.3**	6.1**
	NPDR			NS
OEF	NC	NS	-0.03*	NS
	NDR		-0.04**	NS
	NPDR			0.06**

*P < 0.1; multivariable linear regression, adjusted for age, race, sex, and eye examined
**P ≤ 0.05; multivariable linear regression, adjusted for age, race, sex, and eye examined

Effect of DLFS: Intragroup Comparison

D_A and D_V increased during DLFS in all DR stage groups ($P \leq 0.004$). SO_{2A} did not change with DLFS ($P \geq 0.1$), whereas SO_{2V} increased in NC, NDR and PDR subjects ($P \leq 0.003$). The increase in SO_{2V} approached significance in NPDR subjects ($P = 0.07$). According to changes in SO_{2V} coupled with no change in SO_{2A}, OEF decreased with DLFS in all DR stage groups ($P \leq 0.03$).

Effect of DLFS: Intergroup Comparison

Differences in estimated means of marker ratios between DR stage groups are provided in Table 4.4. D_AR tended to be decreased in NDR compared to NC subjects ($P = 0.09$) and D_VR

tended to be decreased in NPDR compare to NC subjects (P = 0.09). $SO_{2A}R$ did not vary among DR stage groups ($P \geq 0.18$), whereas $SO_{2V}R$ was decreased in NPDR compared to NC and NDR subjects ($P \leq 0.05$). Correspondingly, OEFR was increased in NPDR compared to NC and NDR subjects ($P \leq 0.03$).

TABLE 4.4 DIFFERENCES IN ESTIMATED MEANS OF RETINAL OXYGENATION MARKER RATIOS BETWEEN EACH DIABETIC RETINOPATHY (DR) STAGE GROUP AND A REFERENCE GROUP

Metric Ratios	Reference	DR Stage Group		
		NDR	NPDR	PDR
D_AR	NC	-0.02*	NS	NS
	NDR		NS	NS
	NPDR			NS
D_VR	NC	NS	-0.02*	NS
	NDR		NS	NS
	NPDR			NS
$SO_{2A}R$	NC	NS	NS	NS
	NDR		NS	NS
	NPDR			NS
$SO_{2V}R$	NC	NS	-0.07**	NS
	NDR		-0.05**	NS
	NPDR			NS
OEFR	NC	NS	0.08**	NS
	NDR		0.08**	NS
	NPDR			NS

*P < 0.1; multivariable linear regression, adjusted for age, race, sex, and eye examined
**P ≤ 0.05; multivariable linear regression, adjusted for age, race, sex, and eye examined

Discussion

Using our previously developed optical imaging system, simultaneous measurements of retinal oxygenation markers were obtained before and during DLFS in non-diabetic control and diabetic subjects at stages of DR. Before DLFS and DLFS-induced responses of markers were compared after adjusting for age, race, sex, and eye examined. The results confirmed our

hypothesis that retinal oxygenation markers and their light DLFS-induced responses are altered at stages of DR. D_A was increased in NPDR and PDR and the DLFS-induced vasodilatory responses tended to be decreased in NDR and NPDR. SO_{2A} and SO_{2V} were increased in NDR, NPDR and PDR and $SO_{2V}R$ was diminished in NPDR. Correspondingly, OEF and OEFR were decreased in NPDR subjects.

Effect of DR Stage: Intergroup Comparison

D_A was significantly larger in NPDR as compared to NC and PDR subjects. This finding is consistent with previous studies which found that retinal arterial dilation is related to the incidence of DR[82, 83, 89] However, D_V was not significantly different among DR stage groups in the current study, in contrast to the findings of Klein et al[80] and Kifley et al,[89] who reported that dilation of retinal veins was related to DR progression. The discrepancy between these results is likely due to the smaller sample size in the current study, study design and differences in covariate corrections. SO_{2A} was higher in all DR stage groups compared to NC subjects. Additionally, SO_{2A} was higher in PDR compared to NDR and NPDR subjects. SO_{2V} was higher in NPDR and PDR compared to NC and NDR subjects. These findings are in agreement with previous studies which found increased SO_{2A} and SO_{2V} in DR[4, 90] and increasing SO_{2V} with DR progression.[5, 90, 91]

In NPDR subjects, OEF was significantly lower compared to NDR and PDR, and tended to be lower than NC subjects. Since OEF is defined as the ratio of MO_2 to DO_2,[16] these results indicate differences in MO_2 and DO_2. DO_2 is determined by arterial blood oxygen content and blood flow, which is in turn related to blood vessel diameter. Although DO_2 was not directly measured here, DO_2 was likely increased in NPDR subjects since D_A was larger, consistent with

previous reports of increased retinal blood flow.[92, 93] On the other hand, MO_2 may have been reduced during NPDR. Retinal hypoxia is implicated in DR,[94, 95] which depending on severity, may cause a reduction in MO_2 as shown under severe hypoxia in rats.[96] However, since direct measurement of MO_2 has not previously been reported in DR subjects, a decrease in MO_2 is only speculative. Therefore, it seems likely that the observed reduction of OEF in NPDR was primarily due to an increase in DO_2. In PDR subjects, OEF was not significantly different from that of NC subjects. Since all PDR subjects had received PRP treatment, inner retinal oxygenation was presumably improved [97] due to a loss of oxygen-consuming outer retinal tissue and the resultant increased oxygen flux from the choroidal circulation. Thus, as a result of increased oxygen delivery from the choroid, DO_2 is expected to decrease as the retinal circulation autoregulates. Furthermore, due to the increase in oxygen availability from the choroid and presumably less retinal tissue, inner retinal MO_2 is also decreased. Therefore, the finding of similar OEF between PDR and NC subjects is consistent with decreases to both MO_2 and DO_2.

Effect of DLFS: Intragroup comparison

Increased D_A and D_V in response to DLFS is in agreement with previous studies which demonstrated retinal vasodilation in NC,[16, 23] NDR,[84, 94] NPDR [3, 84] and PDR subjects.[84] SO_{2A} did not respond to DLFS in all DR stage groups, whereas SO_{2V} significantly increased in NC, NDR and PDR subjects and tended to increase in NPDR subjects. These results are in agreement with previous studies which found DLFS did not change SO_{2A} and increased SO_{2V} in NC[16, 23] and NPDR subjects.[3] OEF decreased with DLFS in all DR stage groups, consistent with the findings from Chapter 3.[16] A decrease in OEF indicates that the DLFS-induced augmentation in

DO_2 was greater than that of MO_2.[16] This finding is also in agreement with a recent study by Palkovits et al.[24] which demonstrated DLFS-induced increases in DO_2 (56%) exceeded that of MO_2 (35%) in NC subjects.

Effect of DLFS: Intergroup Comparison

D_AR tended to be lower in NDR compared to NC, in agreement with previous studies using the Dynamic Vessel Analyzer.[94, 95, 98] D_VR tended to be lower in NPDR compared to NC subjects. The vasodilatory findings in the current study are not consistent with previous studies that reported a progressive reduction in D_AR[99] and D_VR[84] with DR stage. Differences in findings may be attributed to the smaller sample size in the current study and differences in covariate corrections.

$SO_{2A}R$ was not different among DR stage groups, while $SO_{2V}R$ was lower in NPDR compared to NC and NDR subjects, in agreement with a previous study.[3] One possible explanation for this observation is based on reduced availability of oxygen to the retinal tissue in NPDR. In the non-disease state, the retinal tissue receives sufficient oxygen and thus, during DLFS-induced augmentations to DO_2, abundant amounts of oxygen are delivered which exceed the change in metabolic demand of the tissue.[24] This results in an increase of SO_{2V} with DLFS and an $SO_{2V}R$ greater than unity. In contrast, tissue that receives insufficient oxygen will extract more when it is made available during the DLFS-induced augmentation of DO_2. This causes a diminished increase in SO_{2V} and a decreased $SO_{2V}R$ compared to normal tissue. Indeed, the vascular pathologies of NPDR, such as capillary shunting [100] and non-perfusion on fluorescein angiography[101, 102] indicate decreased DO_2. In contrast, $SO_{2V}R$ was not significantly different between NC, NDR and PDR subjects. NDR subjects likely had normal retinal oxygenation,

supported in part by the lack of visible vascular pathologies. All PDR subjects had received PRP treatment which likely improved their inner retinal oxygenation such that abundant amounts of oxygen were available during DLFS resulting in an $SO_{2V}R$ similar to that of NC subjects.

At steady state conditions, OEFR quantifies the ratio of DLFS-induced responses in MO_2 to DO_2 without directly measuring either response. OEFR was not significantly different between NC and NDR subjects, despite an observed trend of impaired vasodilatory response, suggesting a diminished DLFS-induced response in DO_2. Together, these results suggest a diminished DLFS-induced response in MO_2 prior to the development of NPDR. OEFR was higher in NPDR compared to NC and NDR, which is likely due to a diminished DLFS-induced response in DO_2, consistent with the observed trend of impaired vasodilatory response. However, a change in the DLFS-induced response of MO_2 cannot be excluded. Interestingly, both OEFR and the vasodilatory responses to DLFS were not significantly different between NC and PDR subjects. This result suggests that PRP treatment may promote the restoration of DLFS-induced responses in DO_2 and MO_2.

There were several limitations to this work. First, since data were acquired by optical imaging techniques, image quality may have affected measurements. However, the system was previously validated and shown to be capable of detecting DLFS-induced changes.[16] Second, OEF quantifies the ratio of MO_2 to DO_2 and cannot directly measure either quantity due to a lack of retinal blood flow measurements. Future studies that simultaneously measure MO_2 and DO_2 at stages of DR are needed to elucidate the underlying reason for a reduced OEF and its DLFS-induced response. Third, a fixed calibration factor was used to calculate vessel diameters[16] and thus did not account for variations in refractive error among subjects. However, subjects with high refractive error, greater than 6 diopters, were excluded from the study. Furthermore, the use

of a constant calibration did not affect diameter measurements compared within subjects or diameter marker ratios compared between subjects. Fourth, there were variations in the clinical history and status of DR subjects. Future studies with a larger sample size that can account for more clinical confounding factors are needed to substantiate the current findings and reveal differences not discernable with this sample size.

In summary, retinal vessel diameters were larger at stages of DR and the DLFS-induced changes tended to be decreased. Oxygen saturation of retinal vessels increased at stages of DR and $SO_{2V}R$ was diminished in NPDR. Correspondingly, OEF and OEFR were decreased in NPDR, suggesting impairment of the MO_2 and DO_2 and their responses to DLFS in DR. These findings of alterations in retinal oxygenation markers and their DLFS-induced responses may help to elucidate the pathophysiology of DR.

V. TECHNIQUES TO ASSESS THE TEMPORAL DYNAMIC RESPONSES OF RETINAL OXYGENATION MARKERS TO DIFFUSE LIGHT FLICKER STIMULATION IN HUMANS

Part 1: Modify the optical imaging system to acquire images before, during and after the cessation of diffuse light flicker stimulation

Introduction

To date, several studies have reported the effects of diffuse light flicker stimulation (DLFS) on retinal oxygenation markers after a specified duration of time,[3, 16, 69] or averaged their temporal dynamic responses to determine a static effect of DLFS on D and retinal blood flow (BF).[25, 103-105] However, some studies have reported non-linear temporal responses of D and BF to DLFS[12, 13, 20, 21, 70] or its cessation[12, 13, 21, 25, 70, 104] and one study qualitatively reported the non-linear responses of oxygen saturation of hemoglobin (SO_2) to DLFS.[23]

These temporal dynamic responses to DLFS and its cessation indicate how the retina accommodates physiological challenges as opposed to the static effect of DLFS, which only provides information on a DLFS-induced steady state. However, to the best of our knowledge, previous studies have only reported the mathematical modeling of temporal dynamic responses of D and BF to DLFS,[21, 26, 106] while the temporal dynamic response of inner retinal oxygen extraction fraction (OEF) to DLFS and its mathematical modeling has not been described.

In the current chapter, the previously developed optical imaging system for simultaneous assessment of retinal oxygenation markers (D, SO_2 and OEF) with DLFS was used to assess the temporal dynamic responses of these markers to DLFS and its cessation. From this assessment,

we propose a mathematical model for the behavior of these temporal dynamics during DLFS. We tested the hypothesis that retinal oxygenation markers respond to DLFS at various time-courses.

Materials and Methods

Subjects

The research study was approved by an Institutional Review Board at the University of Illinois at Chicago. Prior to enrollment, the research study was explained to the subjects and informed consents were obtained according to the tenets of the Declaration of Helsinki. Sixteen healthy subjects (60 ± 12 years; 5 male, 11 female) participated in the study. Exclusion criteria were abnormal retinal examination, history of eye disease or refractive error > 8 diopter. Subjects' pupils were dilated using 1% tropicamide and 2.5% phenylephrine and subjects were seated in front of our modified slit lamp biomicroscope with their heads resting on a chin and forehead support. Light from a light emitting diode was presented to the fellow eye as a fixation target. Subjects were continuously light adapted during imaging due to the instrument's retinal illumination light. Imaging was performed in the right eyes of 12 subjects and the left eyes of 4 subjects. The left eye was selected because of subject's preference (N = 2), reduced visual acuity (N = 1) or choroidal nevus (N = 1) in the right eye. Data were excluded if the coefficient of variation of three repeated measures of D, SO_2 or OEF before DLFS was greater than 0.1.

Instrumentation

The image acquisition protocol and instrument control software of the optical imaging system described in Chapter 3[16] was modified here to assess the temporal dynamic responses of retinal oxygenation markers to DLFS and its cessation. Briefly, a slit lamp biomicroscope was

fitted with a rapid-switching filter wheel containing bandpass filters to illuminate the retina at multiple wavelengths. The optical imaging system provided DLFS stimulation at 10 Hz using light at 530 nm. In the current study, retinal reflectance images at 606 nm and 570 nm wavelengths were acquired periodically every ~13 seconds over a time-course consisting of 29 seconds before DLFS (3 time points), 78 seconds during DLFS (6 time points) and 39 seconds after the cessation of DLFS (3 time points). The schematic diagram of the image acquisition protocol is shown in Figure 5.1.1.

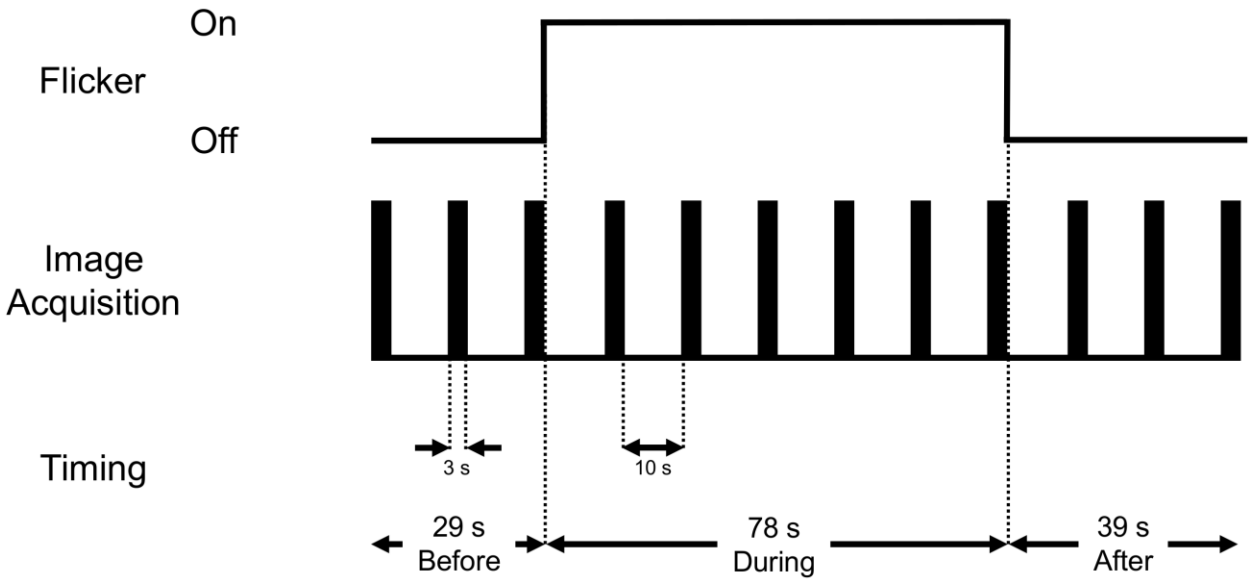

Figure 5.1.1 Schematic of the image acquisition protocol to assess the temporal dynamic responses of retinal oxygenation markers to diffuse light flicker stimulation and its cessation.

At each time point, nine images were acquired at two wavelengths, which were registered and averaged to generate two mean images. These two mean images were then also registered. A circumpapillary region of interest (ROI) extending between one and two disc radii from the perimeter of the optic disc was selected. Measurements of D and SO_2 from each major vessel

within the ROI were obtained and averaged to yield a mean retinal arterial and venous D (D_A, D_V) and SO_2 (SO_{2A}, SO_{2V}), as described in Chapter 3.[16] Inner retinal OEF was calculated as ((SO_{2A}-SO_{2V})/SO_{2A}).[16, 28]

Here, retinal oxygenation marker ratios (D_AR, D_VR, SO_{2A}R, SO_{2V}R, OEFR) were defined as the marker values at each time-point divided by the mean of three repeated metric values obtained before initiation of DLFS. For example, D_AR at the first time-point during DLFS was calculated as $D_{A\_first\ time\text{-}point}$ /$D_{A\_mean\ before\ DLFS}$. Data from all time-points during DLFS and after its cessation were converted to marker ratios for to perform analysis on normalized data.

Data Analysis

Mean and standard deviation (SD) of retinal oxygenation markers from three repeated measurements before DLFS were determined per subject. Intra-subject variability was assessed by coefficient of variation (SD/mean) and averaged over all subjects. Based on data in all subjects, mean and SD of metrics before DLFS were determined and inter-subject variability was calculated by the coefficient of variation. Marker ratios were averaged among subjects at each time-point to generate mean temporal dynamic responses during DLFS and after its cessation. All statistical analyses were performed using SPSS software (version 22, SPSS, Chicago, IL, USA).

Temporal Dynamic Responses to DLFS

We reasoned that, for a well-regulated system like the retina, under a physiological perturbation like DLFS, the rate of change in a marker ratio would be inversely proportional to the deviation of the marker ratio from its value before DLFS. In other words, marker ratio changes occur rapidly at the initiation of DLFS and eventually slow with time as the marker ratio

approaches its DLFS-induced steady state. Therefore, as a first approximation, we used a model in which marker ratios changed during DLFS according to an exponential function, similar to the approach used to evaluate the response of retinal tissue oxygen tension to changes in light levels.[31, 34, 107, 108] General shape of this exponential change in metric ratios during DLFS was given by the following equation:

$$Marker\ Ratio(t) = A + \left(B * \left(1 - e^{-t/C}\right)\right) \quad 5.1.1$$

where t represents time during DLFS, A represents the fitted marker ratio at t=0, B represents the difference in the fitted marker ratio from t=0 to t→∞ (i.e., the maximal DLFS-induced change in the marker ratio), and C represents the time constant, that is the time for the fitted marker ratio to reach $1\text{-}e^{-1}$ (~63%) of the maximal change. Using this notation, the sum of A and B represents the marker ratio at the DLFS-induced steady state.

The temporal dynamic response of each marker ratio was fitted with the aforementioned exponential function using seven data points: a pre-DLFS reference ratio (1.00) and six marker ratio values acquired during DLFS. All data were fit using Matlab 2015 (Mathworks, Natick, MA) to determine values of A, B, C and R^2 for each fitted exponential function.

Temporal Dynamic Response to the Cessation of DLFS

To elucidate the recovery of marker ratios, data acquired at each of the three time-points after the cessation of DLFS were compared to the pre-DLFS reference ratio using one-sample t-tests.

Results

Intra- and inter-subject variability of retinal oxygenation markers were within 5% and 16%, respectively. Mean D_A, D_V, SO_{2A}, SO_{2V} and OEF before DLFS stimulation was 86 ± 7 μm, 105 ± 16 μm, 92 ± 4%, 60 ± 6% and 0.35 ± 0.05, respectively (N = 16). Marker ratios during and after DLFS are provided in Table 5.1.1.

TABLE 5.1.1 RETINAL OXYGENATION MARKER RATIOS (MEAN ± SD) AT SIX TIME-POINTS DURING AND THREE TIME-POINTS AFTER THE CESSATION OF DIFFUSE LIGHT FLICKER STIMULATION

Marker Ratio	**Time from Initiation of Light Flicker (s)**						**Time from Cessation of Light Flicker (s)**		
	13	**26**	**39**	**52**	**65**	**78**	**13**	**26**	**39**
D_AR	1.04 ± 0.05	1.03 ± 0.04	1.05 ± 0.03	1.04 ± 0.03	1.04 ± 0.04	1.06 ± 0.04	1.01 ± 0.04	0.99 ± 0.05	0.98 ± 0.05
D_VR	1.03 ± 0.04	1.05 ± 0.04	1.04 ± 0.04	1.05 ± 0.05	1.05 ± 0.05	1.07 ± 0.03	1.03 ± 0.04	1.02 ± 0.05	1.01 ± 0.02
$SO_{2A}R$	1.00 ± 0.03	1.00 ± 0.03	1.00 ± 0.03	0.99 ± 0.02	0.99 ± 0.02	0.99 ± 0.02	1.00 ± 0.03	1.00 ± 0.02	1.01 ± 0.01
$SO_{2V}R$	1.02 ± 0.06	1.04 ± 0.04	1.04 ± 0.06	1.05 ± 0.05	1.05 ± 0.05	1.07 ± 0.06	1.02 ± 0.07	1.03 ± 0.06	1.01 ± 0.05
OEFR	0.95 ± 0.10	0.92 ± 0.07	0.92 ± 0.09	0.90 ± 0.08	0.90 ± 0.08	0.87 ± 0.09	0.97 ± 0.09	0.96 ± 0.09	1.00 ± 0.08

Temporal Dynamic Responses to DLFS: D_AR and D_VR

Figure 5.1.2 shows the temporal dynamic responses of D_AR and D_VR. For both marker ratios, the exponential function was a good fit ($R^2 \geq 0.87$). From the exponential functions, the DLFS-induced steady state values of D_AR and D_VR were 1.046 and 1.053, respectively, indicating vasodilation of 5% during DLFS. Time constants of exponential fits for D_AR and D_VR were 14 s and 15 s, respectively, indicating relatively rapid vasodilation in response to DLFS. Further, by 78 seconds after the initiation of DLFS, the changes in D_AR and D_VR had reached over 99% of their maximal DLFS-induced changes, as indicated by their exponential fits.

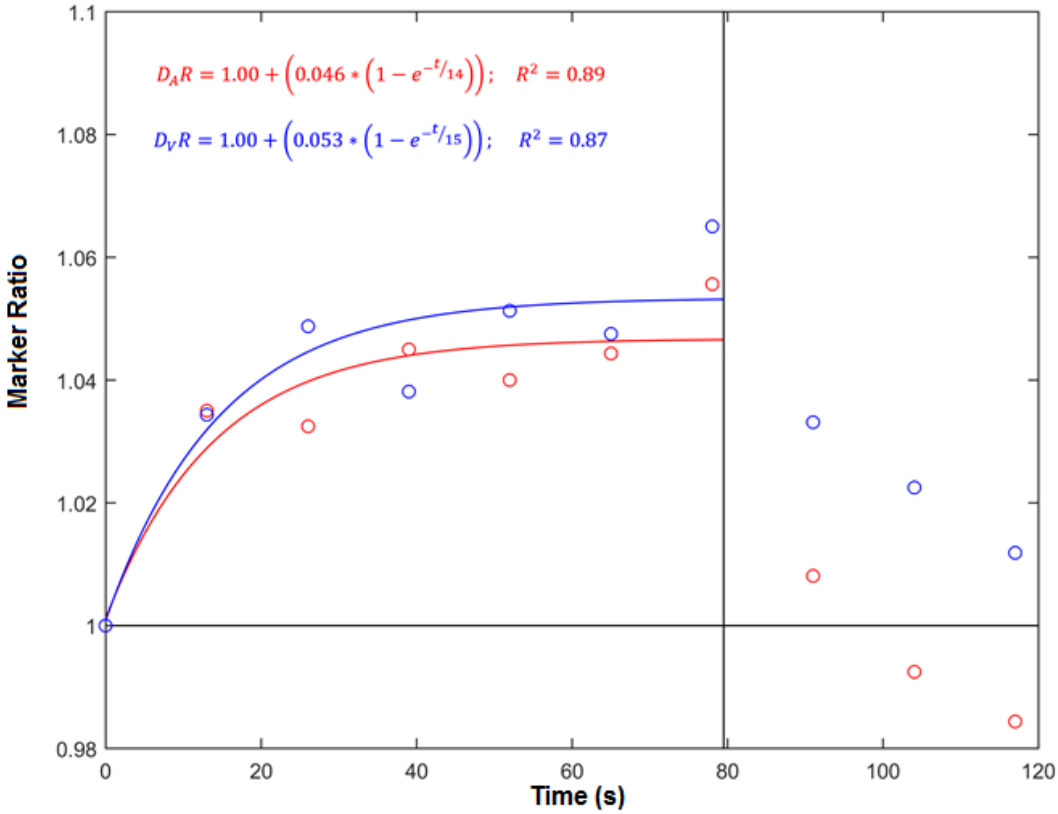

Figure 5.1.2 Marker ratio measurements of retinal arterial and venous diameter (D_AR – red circles; D_VR – blue circles) during diffuse light flicker stimulation and after its cessation. Best-fit exponential functions to both D_AR (red curve) and D_VR (blue curve) during light flicker are shown. The legend provides the exponential functions and R^2 values of D_AR (red) and D_VR (blue). Light flicker begins immediately after t=0 and the vertical black line indicates the time of cessation of light flicker. The horizontal black line indicates a reference ratio of 1.00.

Temporal Dynamic Responses to DLFS: $SO_{2A}R$, $SO_{2V}R$ and OEFR

Figure 5.1.3 shows the temporal dynamic responses of both $SO_{2A}R$ and $SO_{2V}R$, while Figure 5.1.4 shows the temporal dynamic response of OEFR. The exponential functions were excellent fits for both $SO_{2V}R$ and OEFR ($R^2 \geq 0.93$), whereas the fit for $SO_{2A}R$ had a lower R^2 of 0.77. From the exponential functions, the DLFS-induced steady state values of $SO_{2A}R$, $SO_{2V}R$ and OEFR were 0.99, 1.071 and 0.87, respectively. These values indicate a minimal decrease in SO_{2A} of 1%, an increase in SO_{2V} of 7% and a decrease of OEF by 13% during DLFS. Time constants of exponential fits for $SO_{2A}R$, $SO_{2V}R$ and OEFR were 70s, 39s and 34s, respectively. By 78 seconds after the initiation of DLFS, changes in $SO_{2V}R$ and OEFR from the exponential fits had reached nearly 90% of their maximal DLFS-induced changes, whereas the change of $SO_{2A}R$ had only reached 70% of its maximal change.

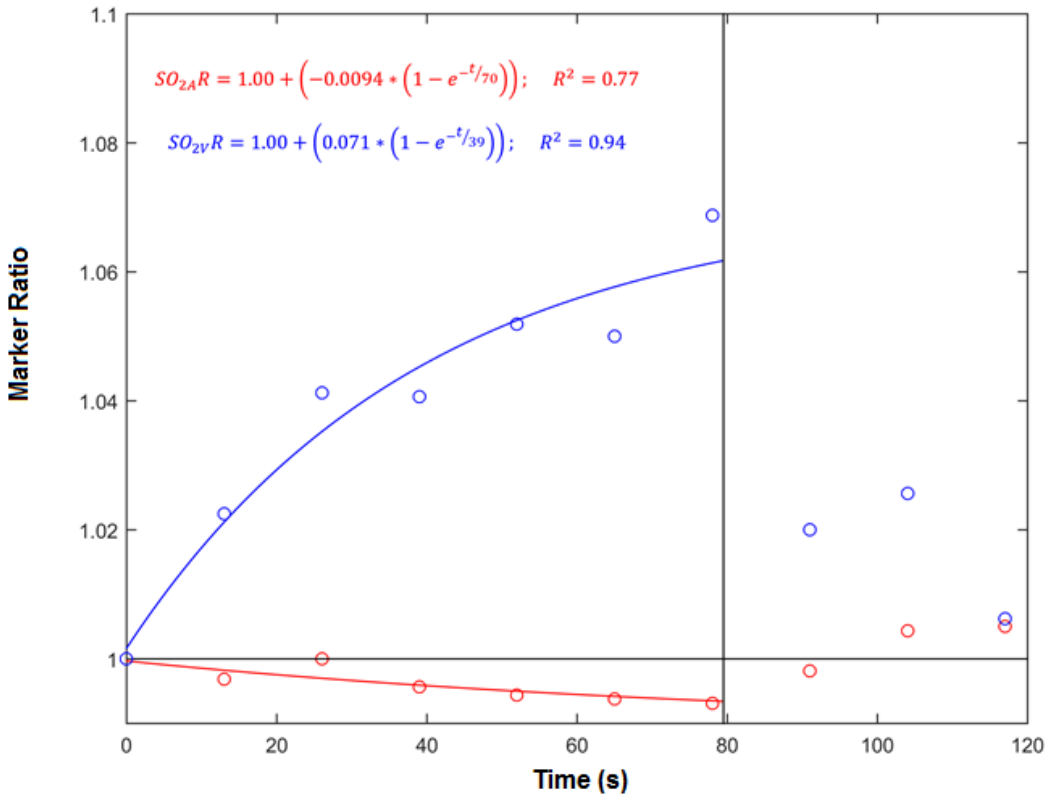

Figure 5.1.3 Marker ratio measurements of retinal arterial and venous oxygen saturation of hemoglobin ($SO_{2A}R$ – red circles; $SO_{2V}R$ – blue circles) during diffuse light flicker stimulation and after its cessation. Best-fit exponential functions to both $SO_{2A}R$ (red curve) and $SO_{2V}R$ (blue curve) during light flicker are shown. The legend provides the exponential functions and R^2 values of $SO_{2A}R$ (red) and $SO_{2V}R$ (blue). Light flicker begins immediately after t=0 and the vertical black line indicates the time of cessation of light flicker. The horizontal black line indicates a reference ratio of 1.00.

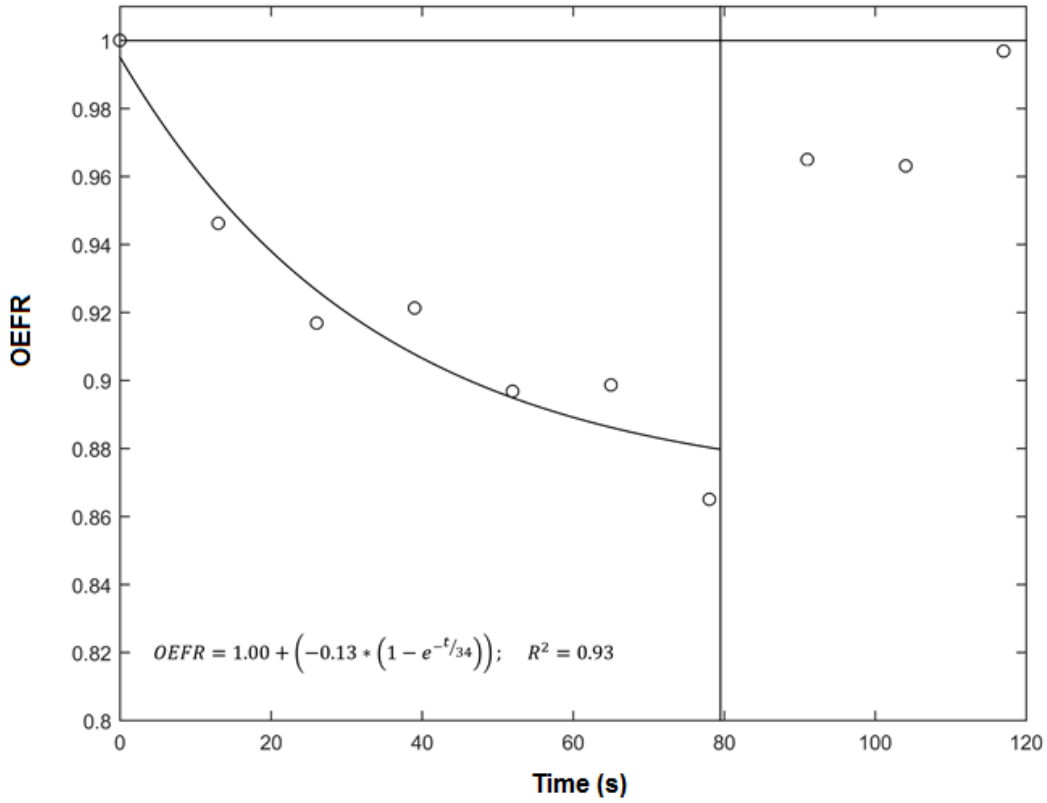

Figure 5.1.4 Marker ratio measurements of inner retinal oxygen extraction fraction (OEFR – circles) during diffuse light flicker stimulation and after its cessation. A best-fit exponential function to OEFR (curve) during light flicker is shown. The legend provides the exponential function and R^2 value of OEFR. Light flicker begins immediately after t=0 and the vertical black line indicates the time of cessation of light flicker. The horizontal black line indicates a reference ratio of 1.00.

Temporal Dynamic Responses to the Cessation of DLFS: D_AR and D_VR

By 13 seconds after the cessation of DLFS, D_AR was not significantly different from the pre-DLFS reference ratio ($P = 0.4$), whereas D_VR remained elevated at 3% ($P < 0.001$) (Figure 5.1.2). However, for all following time-points after the cessation of DLFS, both D_AR and D_VR were not significantly different from the pre-DLFS reference ratio ($P \geq 0.07$).

Temporal Dynamic Responses to the Cessation of DLFS: $SO_{2A}R$, $SO_{2V}R$ and OEFR

By 13 seconds after the cessation of DLFS and at all subsequent time points, $SO_{2A}R$, $SO_{2V}R$ and OEFR were not significantly different from the pre-DLFS reference ratio ($P \geq 0.13$) (Figures 5.1.3 and 5.1.4).

Discussion

In the current study, the combined temporal dynamic responses of retinal oxygenation markers D_A, D_V, SO_{2A}, SO_{2V} and OEF during DLFS and after its cessation were reported in human subjects. To the best of our knowledge, this is the first study to mathematically model the temporal dynamic responses of SO_{2A}, SO_{2V} and OEF.

The DLFS-induced steady values of D_AR and D_VR were 1.046 and 1.053, consistent with previous studies that found vasodilation of a similar magnitude during DLFS.[12, 13, 21, 69, 70, 103] The DLFS-induced steady state values of $SO_{2V}R$ and OEFR were 1.071 and 0.87, in agreement with previous studies which found an increase in SO_{2V}[16, 23] and a decrease in OEF.[16] The DLFS-induced steady state value in $SO_{2A}R$ was 0.99, indicating minimal change in SO_{2A} during DLFS, consistent with previous studies.[16, 23]

The time constants of changes in both D_AR and D_VR in response to DLFS were similar to those reported by previous studies,[21, 26] which substantiates the exponential modeling of the temporal dynamic responses in the current study. The rapid rise time of these markers is also in agreement with a previous study that reported a 10 s time constant for the response of BF at the optic disk to DLFS.[26, 106] Taken together, the time constants of D_AR, D_VR and BF indicate that DO_2 would likely have a similar time constant, resulting in a rapid increase of DO_2 at the initiation of DLFS. Indeed, the ability of DO_2 to increase rapidly during DLFS has been

previously described as a result of complex neurovascular coupling mechanisms.[2, 72, 74] In contrast, the time constants of changes in $SO_{2V}R$ and OEFR in response to DLFS were more than two-fold larger than those of D_AR, D_VR and BF. The apparent mismatch between the supposed time constant of DO_2 and that of OEFR may have important implications concerning the temporal dynamic response of MO_2 to DLFS. However, the use of Fick's principle to quantify OEF as the ratio of MO_2 to DO_2 applies only to steady state conditions,[16, 28] and thus we cannot infer relative changes in MO_2 to DO_2 from OEFR measured during DLFS prior to the establishment of a DLFS-induced steady state. Ultimately, future studies that directly measure the temporal dynamic responses of MO_2 and DO_2 to DLFS are necessary to elucidate the temporal dynamic response of OEFR observed under non-steady state conditions. Nevertheless, this study demonstrates, for the first time, that the time-courses of changes in $SO_{2V}R$ and OEFR to DLFS are considerably different from those of D_AR and D_VR, confirming our hypothesis. Indeed, to achieve 95% of the maximal DLFS-induced change in a metric, a DLFS duration of thrice the time constant is necessary. From the current study, a DLFS duration of 45 s is necessary for changes in D_A and D_V to reach 95% of their maximal DLFS-induced changes, whereas 117 s is necessary for $SO_{2V}R$. Thus, the duration of DLFS should be carefully considered when comparing the results of previous studies, particularly for metrics that have longer time constants.

By 13 seconds after the cessation of DLFS, D_AR, $SO_{2V}R$ and OEFR had returned to pre-DLFS reference ratios, whereas D_VR remained elevated. These findings in D_AR and D_VR are consistent with previous studies that reported minimal arterial vasoconstriction and slight venous vasodilation within 10 seconds after the cessation of DLFS.[12, 13, 21] Although D_AR returned to baseline by about 13 seconds after the cessation of DLFS, the continued elevation of D_VR may

correspond to the phenomenon of delayed venous compliance.[109] Nevertheless, within 26 seconds after the cessation of DLFS, all metric ratios were not significantly different from the reference ratio and the retina had supposedly returned to its pre-DLFS steady state.

There were several limitations in the current study. First, since data were derived based on an optical imaging technique, image quality may have affected measurements. However, inter- and intra-subject variability was low, indicating consistency in measurements. Second, we modeled the complex temporal dynamic responses of metrics to DLFS with a relatively simple exponential equation. Future studies with that assess the temporal dynamic responses with finer temporal resolution may permit better modeling of these phenomena, particularly the temporal dynamic responses of metrics to the cessation of DLFS which could not be modeled here.

In summary, the temporal dynamic responses of OEFR to DLFS and its cessation were reported in human subjects for the first time. The temporal dynamic responses of all markers to DLFS were fit with an exponential function allowing calculation of their DLFS-induced steady state values and time constants. The time constant of the inner retinal oxygen extraction fraction was more than two-fold larger than those of the retinal vascular diameters, indicating considerable differences in the time-courses of responses in these metrics to DLFS. Thus, the duration of flicker should be carefully considered when comparing the results of previous studies. Future application of this technique is potentially useful to elucidate normal physiology and the pathophysiology of retinal diseases.

Part 2: Develop novel optical imaging system for automated, real-time image stabilization

(Parts of) this chapter was (were) previously published as: Anthony E. Felder, Cesare Mercurio, Justin Wanek, Rashid Ansari, Mahnaz Shahidi; Automated Real-Time Conjunctival Microvasculature Image Stabilization. IEEE Trans. Med. Imaging 2016; 35(7):1670-1675.

Introduction

The assessment of temporal dynamics in humans revealed a practical limitation – the loss of imaging data during elongated imaging protocols due to poor subject fixation. Thus, a novel optical imaging system for real-time image stabilization was developed to compensate for subject eye motion. This system was developed in parallel to the one from the previous two Chapters and the image stabilization methodology was validated using human bulbar conjunctiva. This tissue was chosen for its accessibility without the use of dilation drops and relevance to microrcirculatory studies.

The human bulbar conjunctiva is a thin, transparent tissue layer covering the sclera and is densely vascularized. The conjunctiva is easily imaged and thereby permits the study of *in situ* microcirculatory hemodynamics.[110] Previous studies have reported alterations in conjunctival hemodynamics in systemic pathologies including diabetes,[111, 112] Alzheimer's disease,[113] and sickle cell anemia.[114-116] Therefore, assessment of the conjunctival microcirculation is vital to elucidate the pathophysiology of these systemic diseases and how they implicate microvascular hemodynamics.

Several commercially available retinal imaging systems have been modified to assess the hemodynamic properties of the conjunctiva, including the Retinal Functional Imager[117] and

Heidelberg Retinal Flowmeter.[118] Additionally, dedicated optical imaging systems have been developed based on Orthogonal Polarization Spectral imaging,[119] slitlamp biomicroscopy,[110, 114, 120, 121] and intravital microscopy.[112, 122] Image sequences from these systems are acquired at high frame rates and magnifications, and thus require spatial registration prior to quantification of microvascular hemodynamics. However, automated image registration may be hindered by poor image quality and manual image registration requires extensive user interaction and time. Furthermore, both registration methods are applied after image acquisition, resulting in data loss along the boundaries of the imaged area. In contrast, automated real-time image stabilization methodologies that allow for continuous imaging of a conjunctival microvasculature region while maintaining the imaged area would be beneficial for the study of microvascular hemodynamics. Specifically, image stabilization facilitates acquisition of image data over a large microvasculature network region, shortens imaging time for patients, and reduces post-acquisition image processing.

Current retinal imaging systems such as scanning laser ophthalmoscopes[123, 124] and optical coherence tomography systems[125] provide real-time image stabilization using infrared light reflected from the optic disk. However, the optic disk is not visible during conjunctival imaging, making this method of tracking impractical. A single study has used imaging of the conjunctival microvasculature to estimate ocular motion [126], however real-time image stabilization was not attempted.

In the current chapter, we report a novel optical imaging system that performs automated image stabilization of the conjunctival microvasculature by real-time ocular motion tracking and optical path realignment. We tested the hypothesis that real-time image stabilization would maintain imaged area and decrease perceived ocular motion during image acquisition.

Materials and Methods

Subjects

Prior to imaging, the research study was explained to subjects and informed consents were obtained. A total of 5 healthy human subjects (age: 33 ± 11 years; 4 male, 1 female) participated in the study. Subjects were seated in front of the optical imaging system with their head resting on a chin and forehead support. A point source of light was provided as fixation to the right eye while the left eye was imaged. In each subject, between three and four 5-second image sequences of the temporal conjunctival microvasculature were acquired at each image stabilization condition.

Instrumentation

A schematic diagram of the optical imaging system for real-time image stabilization of the conjunctival microvasculature is shown in Figure 5.2.1. The imaging system was assembled on a steel bread board which was mounted on a slit lamp biomicroscope base, allowing precise alignment of the optics with respect to the eye. The white light source from a slit lamp biomicroscope (27 W, BC900, Haag-Streit AG, Koniz, Switzerland) was fitted with a bandpass filter (530 ± 5 nm, Thorlabs, Newton, NJ) to illuminate the conjunctiva at a power of 130 μW. This wavelength was chosen to increase the contrast between the conjunctival microvasculature and the surrounding scleral tissue. Light incident to the eye was reflected by the conjunctiva and directed by two mirrors attached to rotational galvanometers (Model 6240H, Cambridge Tech, Bedford, MA) mounted perpendicular to each other in a customized X-Y mount (Cambridge Tech, Bedford, MA). The galvanometers were powered by two 10 VDC power supplies and controlled using a DAQ board (BNC 2120, National Instruments, Austin, TX) attached to the control computer (Optiplex 990, Windows 7 64-bit, Dell). Rotation of the galvanometers and attached

mirrors in the perpendicular configuration permitted optical beam path realignment in both the horizontal and vertical image dimensions. Light from the conjunctiva was collected by a 150 mm focal length lens (Thorlabs, Newton, NJ) and collimated prior to image path bifurcation. The optical beam path was bifurcated using a 90/10 polarizing pellicle beam splitter (Thorlabs, Newton, NJ). The 10% beam path contained an adjustable aperture and a second 150 mm focus length lens to generate an unmagnified image which was captured by a charge coupled device (CCD) camera (Prosilica GT 1380, Allied Vision Technologies GmbH). This camera acquired 8-bit gray scale images for tracking. The 90% beam path contained the beam expander and camera arm mount of a slitlamp biomicroscope optical head (Zeiss, Jena, Germany) to generate a 3.8x magnified image on a second, identical CCD camera. This camera acquired magnified 8-bit gray scale images for the evaluation of conjunctival hemodynamics and image stabilization. Each camera was controlled by a dedicated GigE network interface card mounted to the control computer's motherboard. Real-time image stabilization and acquisition were controlled using a customized software program (LabView 2014, National Instruments, Austin, TX).

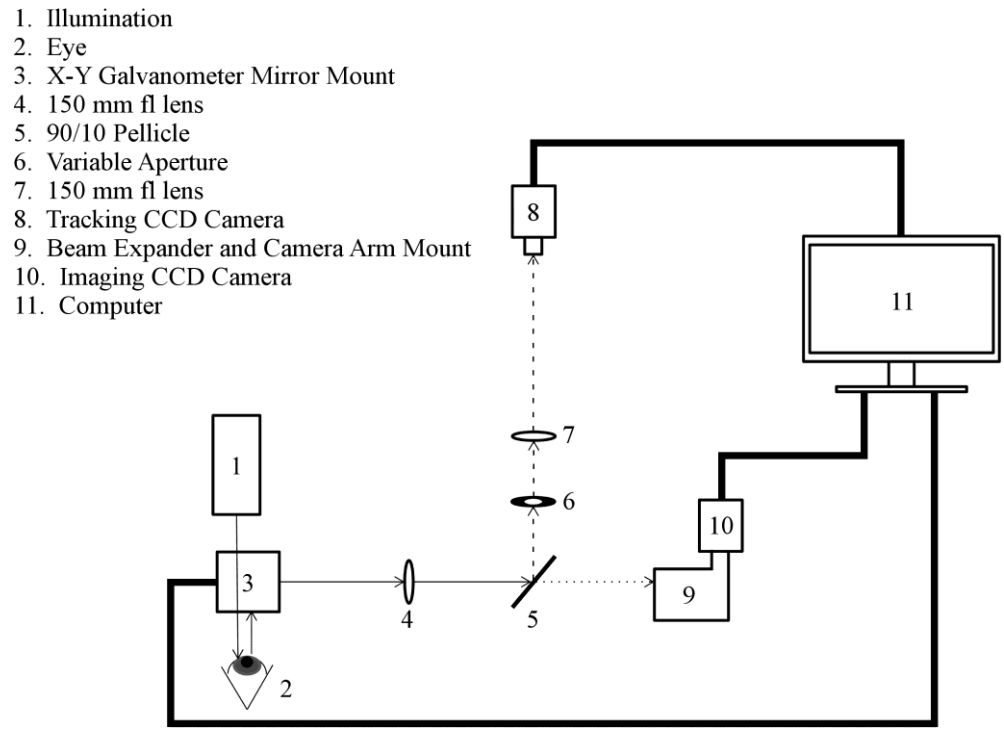

Figure 5.2.1 Schematic diagram of the optical imaging system for automated real-time image stabilization. Thick lines indicate hardware interfaces and thin lines indicate optical beam paths. The dashed and dotted lines indicate the optical beam paths for tracking and imaging, respectively.

Real-time Image Stabilization

The control program simultaneously and independently coordinated image acquisition on both tracking and imaging cameras at different frames per second (FPS) rates. The tracking camera operated at either 60 or 90 FPS by using a region of interest (ROI) on the camera sensor (200x200 pixels; 1.29x1.29 mm), whereas the imaging camera operated at 50 FPS using with a camera sensor ROI (550x550 pixels; 0.94x0.94 mm). Image stabilization was performed in real-time by tracking conjunctival eye motion at one of the two FPS conditions and simultaneously realigning the optical beam path by galvanometer rotation of the two perpendicular mirrors.

Tracking was achieved by determining the displacement of a template image in consecutive tracking camera image frames using a normalized 2D cross correlation algorithm provided by an open source computer vision and machine learning software library[127] (OpenCV,

version 3.0.0). First, the template image was created by cropping the initial tracking camera image frame to a user-assigned ROI of ~50 x 50 pixels. The size of this ROI was chosen to minimize computation load during tracking. Second, the OpenCV cross-correlation function *cvMatchTemplate* generated a 2D array of correlation coefficients by sliding the template image over the current tracking camera image frame in a 2D pixel-wise manner and calculating a correlation coefficient at each location combination. Normalized correlation coefficients were generated by using the normalized matching method argument *CV_TM_CCOEFF_NORMED* within the *cvMatchTemplate* function. Third, the location combination corresponding to the maximum correlation value was used to determine the 2D pixel displacement between the current frame and the first frame which was used to generate the template. The time required to execute the cross correlation algorithm was ~2 ms. If the maximum correlation value was greater than a threshold of 0.7, 2D pixel displacements were converted to galvanometer voltages which were then used to rotate the mirrors in real-time and realign the optical path to stabilize conjunctival microvasculature images. This threshold was determined experimentally based on its ability to provide consistent results during image stabilization of the target. If the maximum correlation value was < 0.7, mirror voltages were not applied and image stabilization temporarily ceased. In this manner, image stabilization could recover from blinks or large saccade if the subject could again fixate on their original target.

Dynamic Response of the Control System

The dynamic response of the control system was characterized by the frequency response, settling time, and steady state displacement error. To characterize these responses, a transparent ruler with millimeter scale precision served as an imaging target. This target was

spatially modulated by applying voltage to a rotating DC motor shaft (Model 50JB, Source Engineering Inc., Santa Clara, CA). Image sequences were acquired before and during image stabilization. The imaging camera's exposure, gain and image acquisition rate were 18 ms, 25, and 50 FPS, respectively. The tracking camera's exposure, gain and image acquisition rate were 11 ms, 31, and 90 FPS, respectively.

The frequency response of the control system was determined by measuring the decibel suppression of target motion during image stabilization. The target was uniaxially modulated by applying voltages from 1 to 21 V (in 1V increments) to the DC motor, producing a spatial oscillation of ~780 μm at frequencies ranging from 0.15 to 2.63 Hz. Image sequences acquired before and during stabilization were used to determine the frequency of the spatial oscillations and the target displacement, respectively. The suppression in target motion was calculated as $-10*\log_{10}(\Delta disp / d_o)$, where $\Delta disp$ was the difference in displacement between before and during image stabilization and d_o was the displacement before image stabilization. A Bode plot of decibel suppression versus target oscillation frequency was generated and fitted with a standard exponential function. The cutoff frequency corresponding to a decibel suppression of -3 dB was measured from the fitted exponential and the frequency response bandwidth was determined.

The settling time of the control system was determined by applying a single, immediate step-wise displacement and tracking image displacement as a function of time during image stabilization. A displacement of 85 μm was applied between successive frames during image stabilization. Image sequences during this displacement were acquired and the settling time was determined as the time required to stabilize the image to within five pixels of the original position.

The steady state displacement error of the control system was determined by performing image stabilization on an immobilized target. Image displacement was averaged over 30 successive image frames and a mean displacement from two repeated measurements was calculated.

Image Stabilization of the Target and Human Conjunctival Microvasculature

Image stabilization was assessed using both a spatially modulated target and the conjunctival microvasculature of human subjects. Image sequences were acquired under three image stabilization conditions: before image stabilization, during image stabilization at 60 FPS, and during image stabilization at 90 FPS. The imaging camera exposure, gain and FPS were 18 ms, 25, and 50 FPS, respectively. The tracking camera exposure, gain and FPS were 11 ms, 31, and 60 or 90 FPS, respectively.

For image stabilization of the target, the target was uniaxially translated by the DC motor at an average speed of 0.9 mm/s. This mean velocity was chosen to represent a substantial challenge to the system without exceeding the cutoff frequency. During translation, three 5-second image sequences were acquired at each image stabilization condition.

For image stabilization of the human conjunctival microvasculature, five human subjects (4 male, 1 female, age = 33 ± 11 years) participated in the current study. Subjects were seated in front of the optical imaging system with their head resting on a chin and forehead support. A fixation target was provided to the right eye while the left eye was imaged. In each subject, between three and four 5-second image sequences of the temporal conjunctival microvasculature were acquired at each image stabilization condition.

Metrics for the Assessment of Image Stabilization

Image stabilization was assessed using three customized metrics: 1) image sharpness, 2) image displacement and 3) field of view. All metrics were quantified using custom algorithms developed in Matlab (Matlab 2013, MathWorks, Natick, MA). First, image sharpness was determined using the mean image generated by averaging all frames from an image sequence. From this mean image, a sharpness score (SS) was calculated by determining the average magnitude of the horizontal and vertical pixel-to-pixel intensity gradients as follows:

$$SS = \sum_{x,y} \left[\left(\frac{\partial I^2}{\partial x} + \frac{\partial I^2}{\partial y} \right)^{1/2} \right] \Big/ N \qquad 5.2.1$$

Here, I(x,y) is the 2D array of intensity values obtained from the mean image, $\partial I^2/\partial x$ and $\partial I^2/\partial y$ are intensity gradients in the x and y dimensions respectively, and N is the number of elements in the 2D array. Higher sharpness scores indicated increased image contrast. Second, frame-to-frame image displacement was determined by tracking a manually defined ROI through the image sequence. The standard deviation of these displacements in both Cartesian image axes (SD_X, SD_Y) were used to calculate the total standard deviation of motion (SD_T) as follows:

$$SD_T = \sqrt{SD_X{}^2 + SD_Y{}^2} \qquad 5.2.2$$

Lower values of SD_T indicate decreased displacement between consecutive image frames and better image stabilization. Third, the field of view during image acquisition was determined using the frame-to-frame displacements measured for the calculation of SD_T. The largest displacements in both Cartesian image axes (D_X, D_Y) were used to calculate the percentage of the field of view that was maintained during image acquisition (FOV_M), according to:

$$FOV_M = \frac{[(I_X - D_X)(I_Y - D_Y)]}{I_X I_Y} * 100 \qquad 5.2.3$$

Here, I_X and I_Y are the image dimensions and in both Cartesian image axes, respectively. Higher values of FOV_M correspond to smaller maximal displacements, indicating a greater maintained field of view and better image stabilization.

The dynamic response of the control system was assessed using the SD_T metric. Target image stabilization was assessed with SS and SD_T metrics. Conjunctival microvasculature image stabilization was assessed using SS, SD_T, and FOV_M metrics.

Data Analysis

Mean SS, SD_T, FOV_M values were calculated by averaging repeated measurements at each image stabilization condition. From conjunctival microvasculature images, the repeatability of SD_T and FOV_M was assessed by calculating the standard deviation of repeated measurements averaged over all subjects at each image stabilization condition. General linear model repeated measures analysis was used to evaluate the effect of image stabilization on stabilization metrics (SS, SD_T, and FOV_M). Pairwise comparisons were performed with Bonferroni adjustments for multiple comparisons. Significance was accepted at $P < 0.05$. SPSS software (version 22, SPSS, Chicago, IL, USA) was used to perform statistical analyses.

Results

Dynamic Response of the Control System

The cutoff frequency of the control system was 2.33 Hz, indicating effective stabilization at mean target velocities of less than 1.82 mm/s. The mean settling time was 328 ± 8 ms, indicating recovery from instantaneous displacements of 85 μm within a third of a second. The steady state displacement error of the system was 0.6 ± 0.2 pixels, corresponding to 1.0 ± 0.3 μm.

Image Stabilization of the Target

Mean images of the target under each image stabilization are shown in Figure 5.2.2A. With successive image stabilization conditions, image contrast and sharpness was visually improved. Mean SS under each image stabilization condition are provided in Figure 5.2.2B. Mean SS values before and during image stabilization at 60 and 90 FPS were 0.54 ± 0.14, 0.70 ± 0.03, 0.77 ± 0.00, respectively. Mean SD_T under each image stabilization condition are provided in Figure 5.2.2C. Before image stabilization, SD_T was 285 ± 16 μm and was 77 ± 1 μm and 60 ± 1 μm during image stabilization at 60 and 90 FPS, respectively.

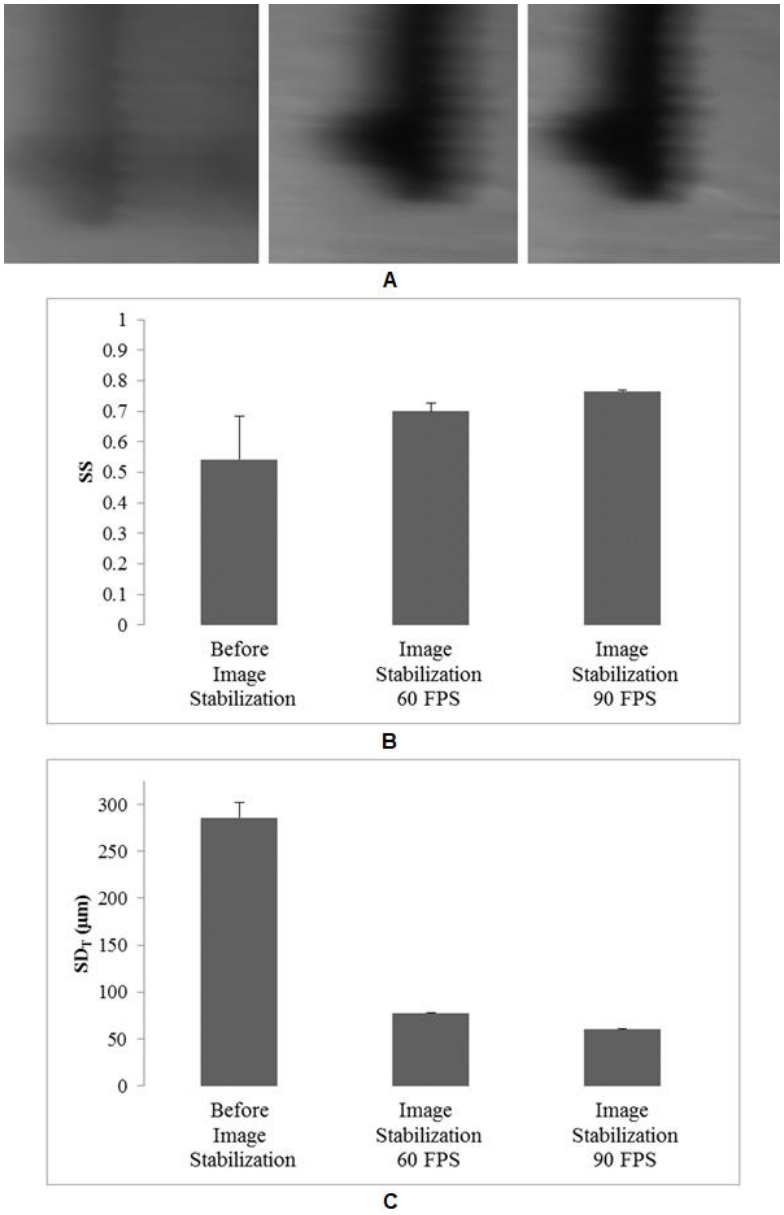

Figure 5.2.2 (A) Mean images of the vertically modulated target at a mean linear velocity of 0.9 mm/s before image stabilization (Left), during image stabilization at 60 FPS (Center), and during image stabilization at 90 FPS (Right). (B) Mean sharpness scores (SS) of the target images at each image stabilization condition. (C) Mean total standard deviation of motion (SD_T) of the target at each image stabilization condition. Error bars indicate standard deviation.

Image Stabilization of Human Conjunctival Microvasculature

Repeatability of SD_T measurements during conjunctival image stabilization at 60 and 90 FPS were 7 µm and 3 µm, respectively. Repeatability of FOV_M measurements during

conjunctival image stabilization at 60 and 90 FPS were 10%, and 3%, respectively. Mean conjunctival microvasculature images from one human subject under each image stabilization condition are shown in Figure 5.2.3A. Similar to the target, conjunctival image stabilization resulted in visibly increased contrast and sharpness resulting in the ability to distinguish fine details, as indicated by arrowhead. Mean SS under each image stabilization condition are provided in Figure 5.2.3B. There was a significant effect of image stabilization on SS ($P = 0.02$), such that image stabilization at 60 and 90 FPS increased SS as compared to before stabilization ($P < 0.05$). However, there was no significant difference in SS between image stabilization at 60 and 90 FPS ($P = 1.0$).

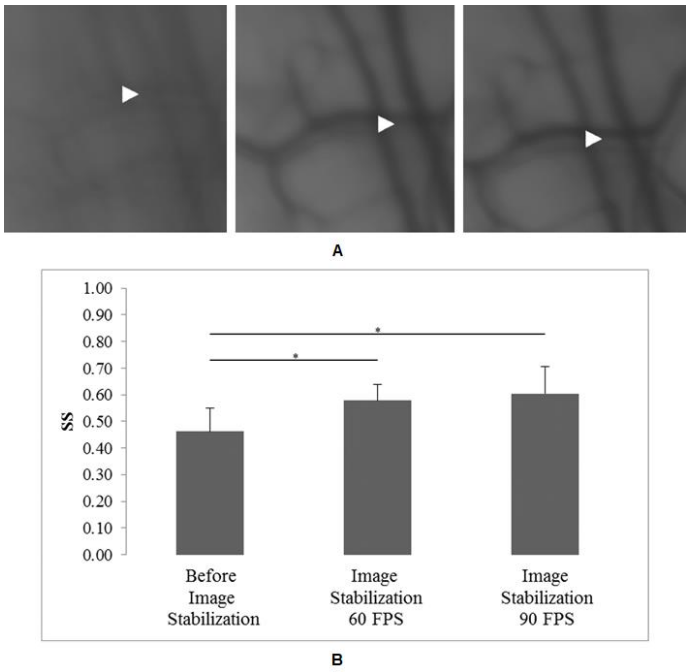

Figure 5.2.3 (A) Mean conjunctival microvasculature images acquired from a representative healthy human subject before (Left) and during image stabilization at 60 FPS (Center) and 90 FPS (Right). Arrowhead indicates area of increased sharpness and contrast, allowing for better visualization of the conjunctival microvasculature. (B) Mean sharpness scores (SS) of conjunctival microvasculature images in human subjects at each image stabilization condition. Error bars and asterisks indicate standard deviation of means and statistically significant differences between stabilization conditions, respectively.

Mean SD_T and FOV_M under each image stabilization condition are provided in Figure 5.2.4A and 5.2.4B, respectively. Before and during image stabilization at 60 and 90 FPS, mean SD_T was 176 ± 24 μm, 39 ± 6 μm and 30 ± 7 μm, respectively. There was a significant effect of image stabilization on SD_T ($P < 0.001$), such that each successive stabilization condition significantly decreased SD_T ($P \leq 0.004$). Mean FOV_M before and during image stabilization at 60 and 90 FPS was 24 ± 11%, 66 ± % and 75 ± 3%, respectively. Image stabilization significantly affected FOV_M ($P = 0.001$), such that each successive stabilization condition significantly increased FOV_M ($P \leq 0.03$).

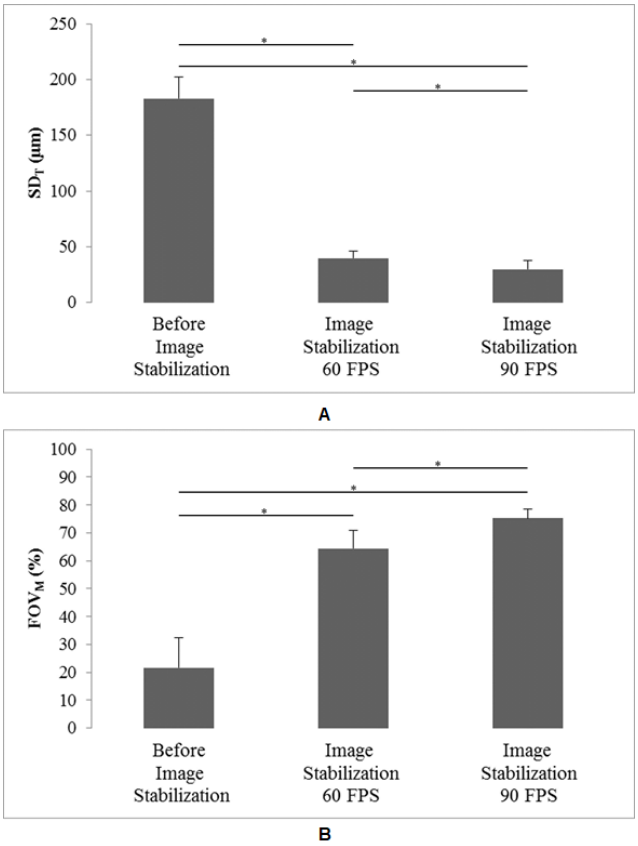

Figure 5.2.4 (A) Mean total standard deviation of motion (SD_T) and (B) mean maintained field of view (FOV_M) of conjunctival microvasculature images in humans at each image stabilization condition. Error bars and asterisks indicate standard deviation of means and statistically significant differences between stabilization conditions, respectively.

Discussion

A novel optical imaging system was developed to perform automated real-time image stabilization of the conjunctival microvasculature. The system uses a normalized cross correlation algorithm to detect conjunctival microvasculature motion and control galvanometer scanners to realign the optical imaging path. Image stabilization was repeatable and reduced displacements of the target and conjunctival microvasculature, while also maintaining a larger field of view of the microvasculature.

The dynamic response of the control system for conjunctival microvasculature image stabilization was established. The cutoff frequency corresponded to a mean velocity of 1.82 mm/s, which is substantially greater than eye motion from saccade and gaze drift.[128] Increased SS of the target image and decreased SD_T during image stabilization were demonstrated, confirming the capability of the system to suppress sustained motion at a velocity within the frequency response of the control system. The settling time of the system was less than a third of a second, adequate to stabilize saccade eye motion which occurs every ~700 ms during fixation and has a latency of ~200 ms.[128, 129]

Conjunctival microvasculature images acquired during image stabilization demonstrated significantly improved visualization of fine details. This observation was confirmed by increased SS and a reduction in SD_T during image stabilization. Furthermore, image stabilization at 90 FPS reduced SD_T to ~30 μm, which was significantly lower than SD_T at 60 FPS. In addition, FOV_M of the conjunctival microvasculature significantly increased during image stabilization. FOV_M was ~75% during image stabilization at 90 FPS, and significantly greater than FOV_M at 60 FPS. These results support the potential of the system to image blood vessels within a fixed region for monitoring of dynamic changes in conjunctival hemodynamics.

In the current configuration, a dedicated optical imaging system was developed for conjunctival microvasculature image stabilization. In the future, such a system may be integrated into the optical imaging system for simultaneous measurement of retinal oxygenation markers with DLFS (Chapter 3). This system for image stabilization would be of particular assistance during the prolonged imaging of the retina to determine the temporal dynamic responses of markers to DLFS (Chapter 5, part 1). It may also be feasible in the future to design and develop a more compact and modular system that can be integrated into commercial slit lamp biomicroscopes, which would facilitate application of this technology for multicenter clinical studies.

There were several limitations to this work. First, image quality affects the system's ability to provide image stabilization. Although image stabilization was demonstrated at high frame rates, image quality can be adversely affected due to the prerequisite short camera exposures. Since the light levels used in the current study were low, a possible solution is to deliver more light to the eye or improve light efficiency along the tracking optical path. Second, since image acquisition and cross correlation occur in series, computation time of the cross correlation algorithm can also directly affect performance. The cross correlation algorithm had a runtime of up to 2 ms and can limit the effective frame rates of both the tracking and imaging cameras. A possible solution is to reduce computation time by performing the cross correlation on the graphics processing unit using compute unified device architecture. Third, this current study established the feasibility of the image stabilization method in a small cohort of healthy subjects. Future studies are needed to determine effects of gender, race, age, and pathologies on the performance of the system.

In summary, a technique for automated real-time image stabilization of the conjunctival microvasculature was demonstrated. This technique was shown to significantly reduce displacements of the target and conjunctival microvasculature as well as maintain the original imaged area during image acquisition. Therefore, this technique may enable further advancements in the study of microvascular pathophysiology. While the optical imaging system was used for stabilized conjunctival microvasculature imaging, the technique described here is applicable to other disciplines and tissues which require image stabilization to further improve the efficacy of image analysis algorithms.

VI. METHODOLOGY FOR THE THREE-DIMENSIONAL IMAGING OF RETINAL OXYGENATION IN RATS

Introduction

Thus far, this thesis has described the assessment of retinal oxygenation markers in humans. It is necessary to assess these non-invasive markers in human studies since current techniques for direct measurement of retinal oxygenation are highly invasive or involve the use of non-native, oxygen-sensitive probes. However, in animal models, measurement of retinal tissue oxygen tension (tPO_2) may be used to directly assess retinal oxygenation.

Oxygen-sensitive microelectrodes directly measure retinal tissue tPO_2 through the retinal depth.[31-34] While the oxygen microelectrode technique is currently considered the best method due to high sensitivity and depth discrimination, it is invasive and provides limited spatial assessment of tPO_2. These limitations were addressed in part by phosphorescence lifetime imaging,[8, 35] which provided non-invasive, depth-resolved measurements of tPO_2 at vertically contiguous retinal locations.[37] However, since this method did not measure retinal tPO_2 in three-dimensions (3D), identification and assessment of physiological and pathological variations in tPO_2 across regions of the retina were limited.

In the current chapter, we address this limitation by volumetric retinal tPO_2 imaging using our previously developed system for the 3D imaging of oxygen tension within the retinal vasculature.[9] This imaging technique overcomes the spatial limitations of existing methods and can provide valuable information about variations in tPO_2 under physiological and pathological conditions.

Materials and Methods

Animals

Nine Long Evans pigmented rats (weight: 300 – 600 g) were used in this study. The animals were treated in compliance with the ARVO Statement for the Use of Animals in Ophthalmic and Vision Research. Anesthesia was induced with intraperitoneal injections of ketamine (100 mg/kg) and xylazine (5 mg/kg), and was maintained during imaging by supplemental doses of ketamine (20 mg/kg) and xylazine (1 mg/kg). An oxygen-sensitive molecular probe, Oxyphor R2 (Oxygen Enterprises, Ltd. Philadelphia, PA) was dissolved in saline and 3 μL (0.5 mM) was injected intravitreally one day prior to imaging, as previously described.[37]

Two separate groups of rats were ventilated mechanically (Harvard Apparatus Inc., South Natick, MA) with either 21%/30% fraction of inspired oxygen (FiO_2) to maintain systemic normoxia (N = 6) or 10% FiO_2 to induce systemic hypoxia (N = 3), as previously reported.[46, 96] One rat from the normoxia cohort was also ventilated under hypoxia for comparative visualization of tPO_2 within the same retinal region. To verify the systemic condition of rats, arterial oxygen tension (P_aO_2), carbon dioxide tension (P_aCO_2), and blood pH were measured by a blood gas analyzer (Radiometer, Westlake, OH or Idexx Vetstat, Westbrook, ME) using blood drawn from a catheter inserted into the femoral artery. Body temperature was maintained at 37ºC using an animal holder with a closed-loop copper tubing water heater. Prior to imaging, pupils were dilated with 2.5% phenylephrine and 1% tropicamide. One percent hydroxypropyl methylcellulose and a glass cover slip were applied to the cornea to eliminate the cornea's refractive power and to prevent corneal dehydration during imaging.

3D Retinal Tissue Oxygen Tension

Our previously described optical section phosphorescence imaging system[9] was used here for the 3D imaging of retinal tPO_2. Briefly, a slitlamp biomicroscope was modified to accommodate a laser (535 nm wavelength, ~40 μW), an optical chopper, a rotational galvonometer with an attached mirror, a high-pass filter with 650 nm cutoff, and an intensified charge-coupled device (ICCD) camera. The laser was projected at an oblique angle to the retina as a ~1 mm vertical line and was modulated by the optical chopper at 1.6 MHz. The laser line was horizontally scanned across the retina and phosphorescence emission was selectively imaged at each location using the high-pass filter placed in front of the ICCD camera. Since the excitation laser and the imaging paths were not coaxial, phosphorescence across the retinal depth appeared laterally displaced in the optical section phosphorescence images.[37] Imaging was performed in one eye of each animal, either temporal or nasal to the optic disc. During imaging, room lights were off and rats were light-adapted due to the scanning laser illumination.

A schematic diagram of the methodology for generating 3D retinal tPO_2 volumes is shown in Figure 6.1. The vertical laser line was horizontally scanned across the retina in 9 μm steps (Figure 6.1A) and optical section phosphorescence images in the y-z plane of the retina were acquired at locations along the x-axis. The number of scan steps ranged from 14-45, dependent on the eye curvature and dilated pupil size. At each retinal scan location, a series of 6 or 10 phase-delayed, optical section phosphorescence images were acquired by setting incremental delays between the modulated laser and intensifier gain of the ICCD camera. Optical section phosphorescence images acquired at each phase delay were stacked along the x-axis to form phase-delayed phosphorescence volumes (Figure 6.1B). The volumes were flattened to remove the effect of the eye curvature and then smoothed by a 3D anisotropic

averaging filter (2 x 6 x 4 pixels in the x, y and z-axes, respectively) (Figure 6.1C). This filter size was selected to smooth each voxel of the phosphorescence volume equally in all dimensions (18 μm x 18 μm x 18 μm). Using a frequency domain technique,[8, 35] phosphorescence lifetime was determined at each voxel from the phase-delayed phosphorescence volumes and PO_2 was then calculated using the Stern-Volmer equation to generate a 3D retinal tPO_2 volume (Figure 6.1D). All image reconstruction and processing was performed using customized algorithms developed in Matlab (MathWorks, Natick, MA).

The chorioretinal and vitreoretinal interfaces were designated from the tPO_2 volume as the location of maximal tPO_2 and 200 μm anterior to the chorioretinal interface[130], respectively. The retinal tPO_2 volume consisted of 45 *en face* tPO_2 images in the x-y plane, extending from the vitreoretinal (*en face* tPO_2 image 1 at retinal depth 0%) to the chorioretinal (*en face* tPO_2 image 45 at retinal depth 100%) interface (Figure 6.1E). The inner and outer retinal volumes were defined as the inner and outer 50% of the total retinal volume and extended from *en face* tPO_2 images 1 to 22 and 23 to 45, respectively.

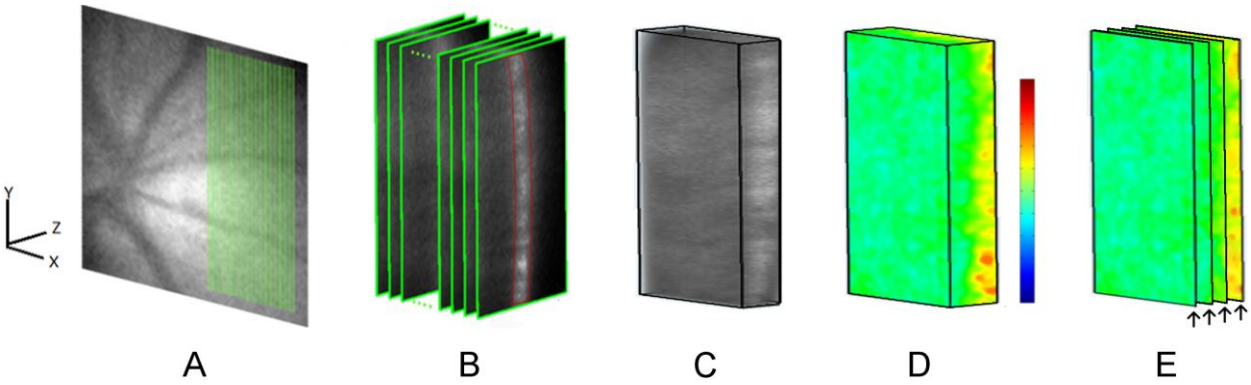

Figure 6.1 A schematic diagram illustrating the steps for the generation of a retinal tissue oxygen tension (tPO_2) volume. (A) A vertical laser line is scanned laterally across the rat retina, as indicated by green lines, to acquire a series of phase-delayed optical section phosphorescence images. (B) The series of zero-phase delay optical section phosphorescence images are stacked along the x-axis. Vertical red lines on the right-most optical section phosphorescence image indicate vitreoretinal (left) and chorioretinal (right) interfaces. (C) The zero-phase delay phosphorescence volume is shown. (D) Using the set of phase-delayed phosphorescence volumes, the phosphorescence lifetime was calculated at each voxel to generate a retinal tPO_2 volume, shown in pseudo color. Color bar indicates tPO_2 between 0 and 50 mmHg. (E) The tPO_2 volume contains 45 *en face* tPO_2 images in x-y planes across the retinal depth. Arrows (from left to right) point to *en face* tPO_2 images at 0%, 33%, 66% and 100% retinal depth.

Data Analysis

From compiled data in all rats, the relationship between mean tPO_2 of *en face* image 45 and systemic P_aO_2 was assessed by linear regression analysis. From each rat and each *en face* tPO_2 depth, the mean tPO_2 ($M_{tPO2,\ rat,\ depth}$) and spatial variation of tPO_2 ($SV_{tPO2,\ rat,\ depth}$) was calculated. Spatial variation represents the variability of tPO_2 in each *en face* image and was calculated as the standard deviation (SD) of tPO_2. Combining measurements of $M_{tPO2,\ rat,\ depth}$ and $SV_{tPO2,\ rat,\ depth}$ from all *en face* images in all rats, M_{tPO2} and SV_{tPO2} depth profiles under each systemic condition were generated. The effects of systemic condition (normoxia, hypoxia) and retinal depth on M_{tPO2} and SV_{tPO2} were determined by mixed linear model. In one retinal region that encompassed both an artery and a vein (vein superior to artery), a mean inner retinal *en face* tPO_2 image (average of *en face* images 1 through 22) was generated and linear regression

analysis was performed between tPO_2 and vertical distance along the image (averaged over 30 μm vertical contiguous regions). This analysis was performed to assess the correlation between inner retinal tPO_2 and location between the artery-vein pair. All statistical analyses were performed using SPSS statistical software (version 22, SPSS, Chicago, IL, USA). Statistical significance was accepted at $P \leq 0.05$.

Results

Qualitative Evaluation of tPO_2 Volumes

All tPO_2 volumes were inspected for qualitatively recognizable characteristics. Representative tPO_2 volumes generated at the same retinal region (indicated in green; Figure 6.2A) in a rat under normoxia (Figure 6.2B) and hypoxia (Figure 6.2C) are shown. As expected, all volumes exhibited greater tPO_2 at the chorioretinal interface compared to the inner retina, and volumes under hypoxia demonstrated lower tPO_2 compared to those under normoxia. Further, tPO_2 volumes appeared relatively uniform, without abrupt variations in tPO_2. Retinal vessels were not visible on most tPO_2 volumes.

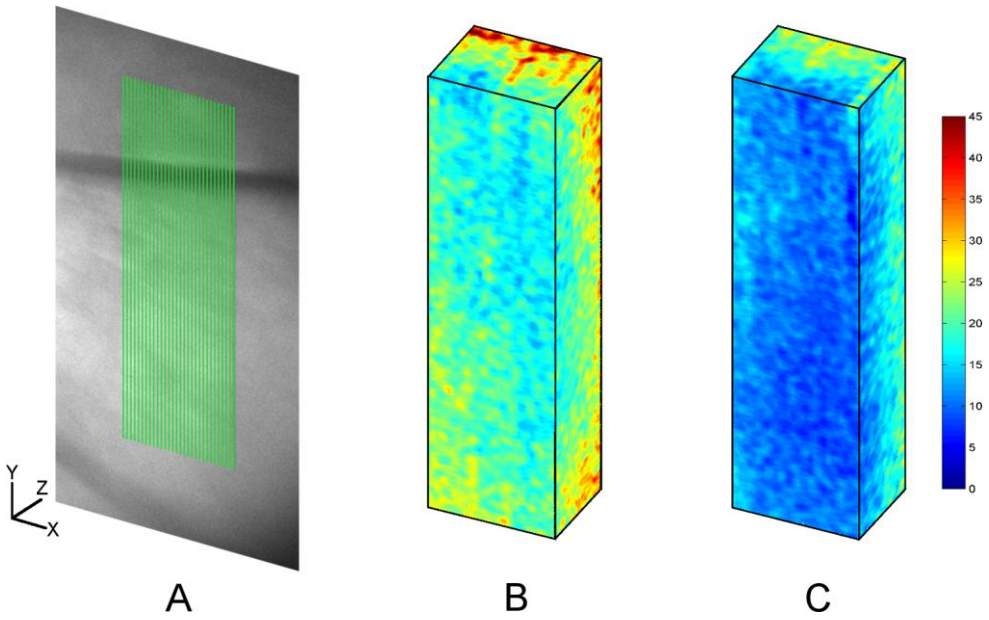

Figure 6.2 (A) Representative retinal region imaged in a rat, indicated by green lines superimposed on the red-free retinal image. Retinal tissue oxygen tension volumes generated in the same retinal region under normoxia (B) and hypoxia (C). Color bar indicates oxygen tension in mmHg.

Quantitative Analysis of tPO_2 Volumes

The P_aO_2, P_aCO_2 and pH levels of rats under systemic normoxia were 95 ± 15 mmHg, 43 ± 13 mmHg, and 7.4 ± 0.15, respectively. For rats under systemic hypoxia, the P_aO_2, P_aCO_2, and pH were 32 ± 3.5 mmHg, 34 ± 5.6 mmHg, and 7.4 ± 0.07, respectively. As shown in Figure 6.3, M_{tPO2} at the chorioretinal interface was linearly correlated with systemic P_aO_2 ($P = 0.007$, $R = 0.82$, $N = 9$).

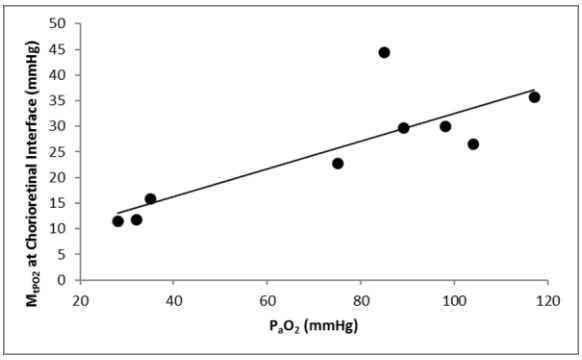

Figure 6.3 Mean retinal tissue oxygen tension (M_{tPO2}) at the chorioretinal interface plotted as a function of systemic arterial oxygen tension (P_aO_2). Compiled data from 9 rats.

Retinal M_{tPO2} depth profiles compiled from data obtained in all rats stratified by systemic condition are shown in Figure 6.4A. At each retinal depth, M_{tPO2} was lower under hypoxia than under normoxia. Under both systemic conditions, M_{tPO2} increased with retinal depth, indicating lower tPO_2 in the inner retina and higher tPO_2 towards the chorioretinal interface. Retinal SV_{tPO2} depth profiles compiled from data obtained in all rats stratified by systemic condition are shown in Figure 6.4B. SV_{tPO2} was lower at each retinal depth under hypoxia as compared to normoxia and highest at the chorioretinal interface under both systemic conditions. There were significant effects of both systemic oxygen condition (normoxia, hypoxia) and retinal depth on both M_{tPO2} and SV_{tPO2} ($P < 0.001$). In a retinal region that encompassed a horizontally-oriented retinal vein superiorly and an artery inferiorly (Figure 2), inner retinal tPO_2 under normoxia decreased along the vertical axis from the inferior artery to the superior vein in a manner well fit by a linear equation ($P < 0.001$, $R = 0.88$, $N = 30$).

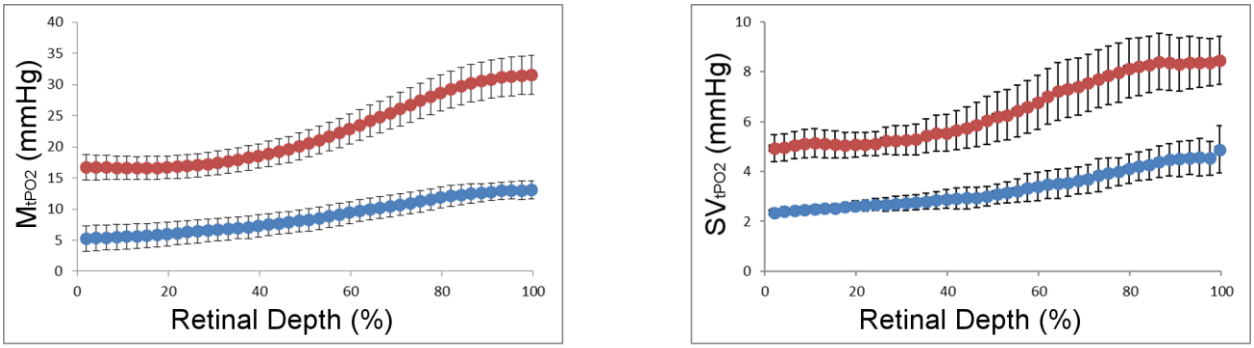

Figure 6.4 (A) Mean retinal tissue oxygen tension (M_{tPO2}) depth profiles under normoxia (Red, N = 6) and hypoxia (Blue, N = 3). (B) Retinal tissue oxygen tension spatial variation (SV_{tPO2}) depth profiles under normoxia (Red) and hypoxia (Blue). Error bars indicate standard error of the means.

Discussion

In the current study, we report a technique for imaging of retinal tissue oxygen tension in three dimensions. Volumetric imaging of retinal tPO_2 is essential to identify and assess the spatial variations of retinal oxygenation which occurs under normal physiological and pathological conditions. Retinal tPO_2 volumes displayed a lower tPO_2 under hypoxia than normoxia, and all volumes displayed greater tPO_2 towards the choroid, as expected. Moreover, tPO_2 in retinal regions appeared relatively uniform (SV_{tPO2} of 5 – 8 mmHg under normoxia), which may be due, at least in part, to the net result of oxygen diffusional gradients within a tissue under steady state. However, despite retention of the oxyphor only in the extra-vascular space, retinal vasculature, which were devoid of phosphorescence signal, could not be visually identified on most tPO_2 volumes. This was mainly due to the scatter of phosphorescence within the retinal tissue.

In the current study, the M_{tPO2} depth profiles compiled from all rats under normoxia demonstrated a large oxygen gradient in the outer retina with the greatest M_{tPO2} occurring at the

chorioretinal interface, consistent with previous studies.[31, 32, 37] This oxygen gradient is necessary to drive oxygen from the choroid to the photoreceptor inner segments.[31, 131] There was also a significant difference in M_{tPO2} at each retinal depth between normoxia and hypoxia, consistent with the findings of previous studies.[37, 42, 132] However, absolute measurements of tPO_2 through the retinal depth were generally lower than those reported in previous studies. In the current study, inner retinal M_{tPO2} and maximal M_{tPO2} under normoxia (18 mmHg, 30 mmHg) were lower than those in light-adapted rats measured by the oxygen microelectrode technique (29 mmHg, 45 mmHg)[32] and phosphorescence lifetime imaging (30 mmHg, 50 mmHg),[37] while they were more comparable to other published values measured using the oxygen microelectrode technique (15 mmHg, 50 mmHg),[31] (13 mmHg, 35 mmHg).[133]

In the current study, we report SV_{tPO2} for the first time, revealing physiologic variations of tPO_2 across retinal regions. Previously, variations in retinal tPO_2 were suggested based on differences in pre-retinal[134-136] and intra-retinal[33, 137] PO_2 measurement between arteries and veins From compiled data in all rats, SV_{tPO2} increased with retinal depth and was greatest towards the choroid (8 mmHg), consistent with previous studies which reported similar variations in rat[32, 37, 130] and cat[34, 42] under light-adapted conditions. Spatial variation of tPO_2 was also depicted by demonstrating a gradient in inner retinal tPO_2 between an artery and vein pair. This can be attributed to the reduction of PO_2 in the microvasculature as blood passes from artery to vein, as well as oxygen diffusion to the retinal tissue between vessels.[58] Additionally, from compiled data in all rats, SV_{tPO2} was lower under hypoxia than normoxia, indicating tPO_2 is less variable during systemic hypoxia. Since the inner retinal tPO_2 range should be related to the difference between the retinal arterial and venous PO_2, a decrease in the arteriovenous PO_2 difference during hypoxia should reduce the SV_{tPO2}. Indeed, a decrease in the retinal

arteriovenous PO_2 difference was previously reported under hypoxia.[96] However, a floor effect on tPO_2 during hypoxia may be present, which can also decrease SV_{tPO2}. Nevertheless, SV_{tPO2} is a valuable metric and may be used to characterize tPO_2 variations across retinal *en face* images for detection of abnormalities, such as retinopathies characterized by multifocal pathologies.

There were several limitations to this work. First, due to the use of laser excitation for phosphorescence lifetime imaging, data can only be obtained in light-adapted rats. Second, intraretinal phosphorescence scattering may reduce depth resolution and alter the tPO_2 depth profiles, though the general trend of tPO_2 retinal depth profiles was similar to that obtained by previous techniques. Third, due to the inverse non-linear relationship between phosphorescence lifetime and tPO_2, this method is less sensitive to the detection of high tPO_2, resulting in greater measurement variability. This limitation may in part account for the observation of higher tPO_2 variability near the choroid. Fourth, eye motion that occurs due to animal respiration during imaging can create shifts between consecutive image locations or blur during a single location. To minimize the contributions of these factors, the phosphorescence volumes were smoothed in post-processing. Smoothing of images decreased variations in the phosphorescence volume, which may have altered calculation of phosphorescence lifetime. However, since comparison of tPO_2 was based on data from multiple animals, this image processing step likely minimally affected the results. Last, the calculation of tPO_2 from phosphorescence lifetime used oxyphor constants that were derived from *ex vivo* experiments, which may be different from those in the retinal tissue. This may affect absolute tPO_2 values, the possibility of which cannot be excluded in this study.

In summary, we demonstrated a technique for the imaging of retinal tissue oxygen tension in three dimensions in rats. This optical imaging technique is a promising tool for detecting spatial variations in retinal tissue oxygen tension in animal models of retinal diseases.

CITED LITERATURE

1. Trick GL, Berkowitz BA. Retinal oxygenation response and retinopathy. *Progress in Retinal and Eye Research* 2005;24:259-274.
2. Kur J, Newman EA, Chan-Ling T. Cellular and physiological mechanisms underlying blood flow regulation in the retina and choroid in health and disease. *Progress in Retinal and Eye Research* 2012;31:377-406.
3. Hammer M, Heller T, Jentsch S, et al. Retinal Vessel Oxygen Saturation under Flicker Light Stimulation in Patients with Non-Proliferative Diabetic Retinopathy. *Invest Ophthalmol Vis Sci* 2012.
4. Hardarson SH, Stefansson E. Retinal oxygen saturation is altered in diabetic retinopathy. *British Journal of Ophthalmology* 2012;96:560-563.
5. Hammer M, Vilser W, Riemer T, et al. Diabetic patients with retinopathy show increased retinal venous oxygen saturation. *Graefes Arch Clin Exp Ophthalmol* 2009;247:1025-1030.
6. Geirsdottir A, Hardarson SH, Olafsdottir OB, Stefansson E. Retinal oxygen metabolism in exudative age-related macular degeneration. *Acta Ophthalmologica* 2014;92:27-33.
7. Olafsdottir OB, Vandewalle E, Abegao Pinto L, et al. Retinal oxygen metabolism in healthy subjects and glaucoma patients. *Br J Ophthalmol* 2014;98:329-333.
8. Shonat RD, Kight AC. Oxygen tension imaging in the mouse retina. *Ann Biomed Eng* 2003;31:1084-1096.
9. Shahidi M, Wanek J, Blair NP, Mori M. Three-dimensional mapping of chorioretinal vascular oxygen tension in the rat. *Invest Ophthalmol Vis Sci* 2009;50:820-825.

10. Wilson DF, Vinogradov SA, Grosul P, Kuroki A, Bennett J. Imaging oxygen pressure in the retina of the mouse eye. *Adv Exp Med Biol* 2005;566:159-165.

11. Hammer M, Vilser W, Riemer T, Schweitzer D. Retinal vessel oximetry-calibration, compensation for vessel diameter and fundus pigmentation, and reproducibility. *Journal of Biomedical Optics* 2008;13.

12. Lanzl IM, Seidova SF, Maier M, et al. Dynamic retinal vessel response to flicker in age-related macular degeneration patients before and after vascular endothelial growth factor inhibitor injection. *Acta Ophthalmol* 2011;89:472-479.

13. Heitmar R, Summers RJ. The Time Course of Changes in Retinal Vessel Diameter in Response to Differing Durations of Flicker Light Provocation. *Invest Ophthalmol Vis Sci* 2015;56:7581-7588.

14. Delori FC. Noninvasive technique for oximetry of blood in retinal vessels. *Appl Opt* 1988;27:1113-1125.

15. Beach JM, Schwenzer KJ, Srinivas S, Kim D, Tiedeman JS. Oximetry of retinal vessels by dual-wavelength imaging: calibration and influence of pigmentation. *J Appl Physiol (1985)* 1999;86:748-758.

16. Felder AE, Wanek J, Blair NP, Shahidi M. Inner Retinal Oxygen Extraction Fraction in Response to Light Flicker Stimulation in Humans. *Invest Ophthalmol Vis Sci* 2015;56:6633-6637.

17. Beach J. Pathway to Retinal Oximetry. *Transl Vis Sci Technol* 2014;3:2.

18. Song W, Wei Q, Liu W, et al. A combined method to quantify the retinal metabolic rate of oxygen using photoacoustic ophthalmoscopy and optical coherence tomography. *Sci Rep* 2014;4:6525.

19. Yi J, Wei Q, Liu W, Backman V, Zhang HF. Visible-light optical coherence tomography for retinal oximetry. *Opt Lett* 2013;38:1796-1798.

20. Falsini B, Riva CE, Logean E. Flicker-evoked changes in human optic nerve blood flow: Relationship with retinal neural activity. *Investigative Ophthalmology & Visual Science* 2002;43:2309-2316.

21. Polak K, Schmetterer L, Riva CE. Influence of flicker frequency on flicker-induced changes of retinal vessel diameter. *Investigative Ophthalmology & Visual Science* 2002;43:2721-2726.

22. Garhofer G, Bek T, Boehm AG, et al. Use of the retinal vessel analyzer in ocular blood flow research. *Acta Ophthalmologica* 2010;88:717-722.

23. Hammer M, Vilser W, Riemer T, et al. Retinal venous oxygen saturation increases by flicker light stimulation. *Invest Ophthalmol Vis Sci* 2011;52:274-277.

24. Palkovits S, Lasta M, Told R, et al. Relation of retinal blood flow and retinal oxygen extraction during stimulation with diffuse luminance flicker. *Sci Rep* 2015;5:18291.

25. Garhofer G, Zawinka C, Resch H, Huemer KH, Dorner GT, Schmetterer L. Diffuse luminance flicker increases blood flow in major retinal arteries and veins. *Vision Research* 2004;44:833-838.

26. Riva CE, Logean E, Falsini B. Visually evoked hemodynamical response and assessment of neurovascular coupling in the optic nerve and retina. *Progress in Retinal and Eye Research* 2005;24:183-215.

27. Ito H, Kanno I, Kato C, et al. Database of normal human cerebral blood flow, cerebral blood volume, cerebral oxygen extraction fraction and cerebral metabolic rate of oxygen measured by positron emission tomography with O-15-labelled carbon dioxide or water,

carbon monoxide and oxygen: a multicentre study in Japan. *European Journal of Nuclear Medicine and Molecular Imaging* 2004;31:635-643.

28. Teng PY, Wanek J, Blair NP, Shahidi M. Inner retinal oxygen extraction fraction in rat. *Invest Ophthalmol Vis Sci* 2013;54:647-651.

29. Felder AE, Wanek J, Blair NP, et al. The Effects of Diabetic Retinopathy Stage and Light Flicker on Inner Retinal Oxygen Extraction Fraction. *Invest Ophthalmol Vis Sci* 2016;57:5586-5592.

30. Felder A, Mercurio C, Wanek J, Ansari R, Shahidi M. Automated Real-time Conjunctival Microvasculature Image Stabilization. *IEEE Trans Med Imaging* 2016.

31. Cringle SJ, Yu DY, Yu PK, Su EN. Intraretinal oxygen consumption in the rat in vivo. *Invest Ophthalmol Vis Sci* 2002;43:1922-1927.

32. Lau JC, Linsenmeier RA. Oxygen consumption and distribution in the Long-Evans rat retina. *Exp Eye Res* 2012;102:50-58.

33. Pournaras CJ, Riva CE, Tsacopoulos M, Strommer K. Diffusion of O2 in the retina of anesthetized miniature pigs in normoxia and hyperoxia. *Exp Eye Res* 1989;49:347-360.

34. Braun RD, Linsenmeier RA, Goldstick TK. Oxygen consumption in the inner and outer retina of the cat. *Invest Ophthalmol Vis Sci* 1995;36:542-554.

35. Shahidi M, Shakoor A, Blair NP, Mori M, Shonat RD. A method for chorioretinal oxygen tension measurement. *Curr Eye Res* 2006;31:357-366.

36. Shonat RD, Norige AS. Developing strategies for three-dimensional imaging of oxygen tension in the rodent retina. *Adv Exp Med Biol* 2005;566:173-178.

37. Shahidi M, Wanek J, Blair NP, Little DM, Wu T. Retinal Tissue Oxygen Tension Imaging in Rat. *Investigative ophthalmology & visual science* 2010;09-4710.

38. *Encyclopedia of the Eye*: Elsevier; 2010.

39. Berne RM, Levy MN, Koeppen BM, Stanton BA. *Berne & Levy physiology*. 6th ed. Philadelphia, PA: Mosby/Elsevier; 2008:xii, 834 p.

40. Lehninger AL, Nelson DL, Cox MM. *Lehninger principles of biochemistry*. 5th ed. New York: W.H. Freeman; 2008.

41. Boron WF, Boulpaep EL. *Medical physiology : a cellular and molecular approach*. 2nd ed. Philadelphia, PA: Saunders/Elsevier; 2009:xii, 1337 p.

42. Linsenmeier RA, Braun RD. Oxygen distribution and consumption in the cat retina during normoxia and hypoxemia. *J Gen Physiol* 1992;99:177-197.

43. Pittman RN. Oxygen Transport in Normal and Pathological Situations: Defects and Compensations. In: Pittman RN (ed), *Regulation of Tissue Oxygenation.* San Rafael, CA: Morgan & Claypool Life Sciences; 2011:47-50.

44. Baron JC, Bousser MG, Rey A, Guillard A, Comar D, Castaigne P. Reversal of focal "misery-perfusion syndrome" by extra-intracranial arterial bypass in hemodynamic cerebral ischemia. A case study with 15O positron emission tomography. *Stroke* 1981;12:454-459.

45. Yamauchi H, Fukuyama H, Nagahama Y, et al. Significance of increased oxygen extraction fraction in five-year prognosis of major cerebral arterial occlusive diseases. *J Nucl Med* 1999;40:1992-1998.

46. Teng PY, Wanek J, Blair NP, Shahidi M. Response of Inner Retinal Oxygen Extraction Fraction to Light Flicker Under Normoxia and Hypoxia in Rat. *Investigative Ophthalmology & Visual Science* 2014;55:6055-6058.

47. Cringle SJ, Yu DY, Alder VA, Su EN, Yu PK. Quantification of retinal oxygen consumption changes from preretinal oxygen transients. *Aust N Z J Ophthalmol* 1998;26 Suppl 1:S71-73.

48. Crystal GJ. Principles of cardiovascular physiology. In: Estafanous FG, Barash PG, Reves JG (eds), *Cardiac anesthesia: principles and clinical practice.* Philadelphia, PA, USA: Lippincott Williams & Wilkins; 2001:37-57.

49. Zijlstra WG, Buursma A, Meeuwsen-van der Roest WP. Absorption spectra of human fetal and adult oxyhemoglobin, de-oxyhemoglobin, carboxyhemoglobin, and methemoglobin. *Clin Chem* 1991;37:1633-1638.

50. Hickam JB, Frayser R, Ross JC. A study of retinal venous blood oxygen saturation in human subjects by photographic means. *Circulation* 1963;27:375-385.

51. Hardarson SH. Retinal oximetry. *Acta Ophthalmol* 2013;91 Thesis 2:1-47.

52. Wilson DF. Oxygen dependent quenching of phosphorescence: a perspective. *Adv Exp Med Biol* 1992;317:195-201.

53. Shonat RD, Wilson DF, Riva CE, Cranstoun SD. Effect of acute increases in intraocular pressure on intravascular optic nerve head oxygen tension in cats. *Invest Ophthalmol Vis Sci* 1992;33:3174-3180.

54. Shonat RD, Wilson DF, Riva CE, Pawlowski M. Oxygen distribution in the retinal and choroidal vessels of the cat as measured by a new phosphorescence imaging method. *Appl Opt* 1992;31:3711-3718.

55. Lakowicz JR, Szmacinski H, Nowaczyk K, Johnson ML. Fluorescence Lifetime Imaging of Free and Protein-Bound Nadh. *Proceedings of the National Academy of Sciences of the United States of America* 1992;89:1271-1275.

56. Shakoor A, Blair NP, Mori M, Shahidi M. Chorioretinal vascular oxygen tension changes in response to light flicker. *Invest Ophthalmol Vis Sci* 2006;47:4962-4965.

57. Lo LW, Koch CJ, Wilson DF. Calibration of oxygen-dependent quenching of the phosphorescence of Pd-meso-tetra (4-carboxyphenyl) porphine: a phosphor with general application for measuring oxygen concentration in biological systems. *Anal Biochem* 1996;236:153-160.

58. Teng PY, Blair NP, Wanek J, Shahidi M. Oxygen tension and gradient measurements in the retinal microvasculature of rats. *Graefes Arch Clin Exp Ophthalmol* 2012;250:361-367.

59. Dunphy I, Vinogradov SA, Wilson DF. Oxyphor R2 and G2: phosphors for measuring oxygen by oxygen-dependent quenching of phosphorescence. *Anal Biochem* 2002;310:191-198.

60. Hardarson SH, Harris A, Karlsson RA, et al. Automatic retinal oximetry. *Investigative Ophthalmology & Visual Science* 2006;47:5011-5016.

61. Blondal R, Sturludottir MK, Hardarson SH, Halldorsson GH, Stefansson E. Reliability of vessel diameter measurements with a retinal oximeter. *Graefes Arch Clin Exp Ophthalmol* 2011;249:1311-1317.

62. Geirsdottir A, Palsson O, Hardarson SH, Olafsdottir OB, Kristjansdottir JV, Stefansson E. Retinal Vessel Oxygen Saturation in Healthy Individuals. *Investigative Ophthalmology & Visual Science* 2012;53:5433-5442.

63. Riva CE, Falsini B, Logean E. Flicker-evoked responses of human optic nerve head blood flow: Luminance versus chromatic modulation. *Investigative Ophthalmology & Visual Science* 2001;42:756-762.

64. Moss HE, Treadwell G, Wanek J, DeLeon S, Shahidi M. Retinal vessel diameter assessment in papilledema by semi-automated analysis of SLO images: feasibility and reliability. *Invest Ophthalmol Vis Sci* 2014;55:2049-2054.

65. Frangi AF, Niessen WJ, Vincken KL, Viergever MA. Multiscale vessel enhancement filtering. *Medical Image Computing and Computer-Assisted Intervention - Miccai'98* 1998;1496:130-137.

66. Pedersen L, Grunkin M, Ersboll B, et al. Quantitative measurement of changes in retinal vessel diameter in ocular fundus images. *Pattern Recognition Letters* 2000;21:1215-1223.

67. Quigley HA, Brown AE, Morrison JD, Drance SM. The size and shape of the optic disc in normal human eyes. *Arch Ophthalmol* 1990;108:51-57.

68. Kristjansdottir JV, Hardarson SH, Halldorsson GH, Karlsson RA, Eliasdottir TS, Stefansson E. Retinal oximetry with a scanning laser ophthalmoscope. *Invest Ophthalmol Vis Sci* 2014;55:3120-3126.

69. Formaz F, Riva CE, Geiser M. Diffuse luminance flicker increases retinal vessel diameter in humans. *Current Eye Research* 1997;16:1252-1257.

70. Nagel E, Vilser W. Flicker observation light induces diameter response in retinal arterioles: a clinical methodological study. *Br J Ophthalmol* 2004;88:54-56.

71. Palkovits S, Told R, Boltz A, et al. Effect of increased oxygen tension on flicker-induced vasodilatation in the human retina. *Journal of cerebral blood flow and metabolism : official journal of the International Society of Cerebral Blood Flow and Metabolism* 2014;34:1914-1918.

72. Roy CS, Sherrington CS. On the Regulation of the Blood-supply of the Brain. *J Physiol* 1890;11:85-158 117.

73. Attwell D, Buchan AM, Charpak S, Lauritzen M, Macvicar BA, Newman EA. Glial and neuronal control of brain blood flow. *Nature* 2010;468:232-243.

74. Newman EA. Functional hyperemia and mechanisms of neurovascular coupling in the retinal vasculature. *Journal of Cerebral Blood Flow and Metabolism* 2013;33:1685-1695.

75. Palkovits S, Lasta M, Told R, et al. Retinal oxygen metabolism during normoxia and hyperoxia in healthy subjects. *Invest Ophthalmol Vis Sci* 2014;55:4707-4713.

76. Wang L, Bill A. Effects of constant and flickering light on retinal metabolism in rabbits. *Acta Ophthalmologica Scandinavica* 1997;75:227-231.

77. Ames A, Li YY, Heher EC, Kimble CR. Energy-Metabolism of Rabbit Retina as Related to Function - High Cost of Na+ Transport. *Journal of Neuroscience* 1992;12:840-853.

78. Fong DS, Aiello L, Gardner TW, et al. Diabetic retinopathy. *Diabetes Care* 2003;26:226-229.

79. Centers for Disease Control and Prevention. National Diabetes Statistics Report: Estimates of Diabetes and Its Burden in the United States. In: Services DoHaH (ed). Atlanta, GA, U.S.; 2014.

80. Klein R, Klein BE, Moss SE, et al. The relation of retinal vessel caliber to the incidence and progression of diabetic retinopathy: XIX: the Wisconsin Epidemiologic Study of Diabetic Retinopathy. *Arch Ophthalmol* 2004;122:76-83.

81. Klein R, Klein BE, Moss SE, Wong TY. Retinal vessel caliber and microvascular and macrovascular disease in type 2 diabetes: XXI: the Wisconsin Epidemiologic Study of Diabetic Retinopathy. *Ophthalmology* 2007;114:1884-1892.

82. Cheung N, Rogers SL, Donaghue KC, Jenkins AJ, Tikellis G, Wong TY. Retinal arteriolar dilation predicts retinopathy in adolescents with type 1 diabetes. *Diabetes Care* 2008;31:1842-1846.

83. Rogers SL, Tikellis G, Cheung N, et al. Retinal arteriolar caliber predicts incident retinopathy: the Australian Diabetes, Obesity and Lifestyle (AusDiab) study. *Diabetes Care* 2008;31:761-763.

84. Lim LS, Ling LH, Ong PG, et al. Dynamic responses in retinal vessel caliber with flicker light stimulation in eyes with diabetic retinopathy. *Invest Ophthalmol Vis Sci* 2014;55:5207-5213.

85. Nguyen TT, Kawasaki R, Kreis AJ, et al. Correlation of light-flicker-induced retinal vasodilation and retinal vascular caliber measurements in diabetes. *Invest Ophthalmol Vis Sci* 2009;50:5609-5613.

86. Nguyen TT, Wang JJ, Sharrett AR, et al. Relationship of retinal vascular caliber with diabetes and retinopathy: the Multi-Ethnic Study of Atherosclerosis (MESA). *Diabetes Care* 2008;31:544-549.

87. Introduction to SAS. http://www.ats.ucla.edu/stat/sas/notes2/: UCLA: Statistical Consulting Group; 2007.

88. Hidalgo B, Goodman M. Multivariate or multivariable regression? *Am J Public Health* 2013;103:39-40.

89. Kifley A, Wang JJ, Cugati S, Wong TY, Mitchell P. Retinal vascular caliber, diabetes, and retinopathy. *Am J Ophthalmol* 2007;143:1024-1026.

90. Jorgensen CM, Hardarson SH, Bek T. The oxygen saturation in retinal vessels from diabetic patients depends on the severity and type of vision-threatening retinopathy. *Acta Ophthalmol* 2014;92:34-39.

91. Khoobehi B, Firn K, Thompson H, Reinoso M, Beach J. Retinal Arterial and Venous Oxygen Saturation Is Altered in Diabetic Patients. *Investigative Ophthalmology & Visual Science* 2013;54:7103-7106.

92. Schmetterer L, Wolzt M. Ocular blood flow and associated functional deviations in diabetic retinopathy. *Diabetologia* 1999;42:387-405.

93. Cuypers MH, Kasanardjo JS, Polak BC. Retinal blood flow changes in diabetic retinopathy measured with the Heidelberg scanning laser Doppler flowmeter. *Graefes Arch Clin Exp Ophthalmol* 2000;238:935-941.

94. Lasta M, Pemp B, Schmidl D, et al. Neurovascular dysfunction precedes neural dysfunction in the retina of patients with type 1 diabetes. *Invest Ophthalmol Vis Sci* 2013;54:842-847.

95. Garhofer G, Zawinka C, Resch H, Kothy P, Schmetterer L, Dorner GT. Reduced response of retinal vessel diameters to flicker stimulation in patients with diabetes. *British Journal of Ophthalmology* 2004;88:887-890.

96. Wanek J, Teng PY, Blair NP, Shahidi M. Inner retinal oxygen delivery and metabolism under normoxia and hypoxia in rat. *Invest Ophthalmol Vis Sci* 2013;54:5012-5019.

97. Budzynski E, Smith JH, Bryar P, Birol G, Linsenmeier RA. Effects of photocoagulation on intraretinal PO2 in cat. *Invest Ophthalmol Vis Sci* 2008;49:380-389.

98. Lecleire-Collet A, Audo I, Aout M, et al. Evaluation of retinal function and flicker light-induced retinal vascular response in normotensive patients with diabetes without retinopathy. *Invest Ophthalmol Vis Sci* 2011;52:2861-2867.

99. Mandecka A, Dawczynski J, Blum M, et al. Influence of flickering light on the retinal vessels in diabetic patients. *Diabetes Care* 2007;30:3048-3052.

100. Leopold IH. Capillary Shunts in the Pathogenesis of Diabetic Retinopathy. *Diabetes* 1963;12:349-350.

101. Shimizu K, Kobayashi Y, Muraoka K. Midperipheral fundus involvement in diabetic retinopathy. *Ophthalmology* 1981;88:601-612.

102. Niki T, Muraoka K, Shimizu K. Distribution of capillary nonperfusion in early-stage diabetic retinopathy. *Ophthalmology* 1984;91:1431-1439.

103. Garhofer G, Zawinka C, Huemer KH, Schmetterer L, Dorner GT. Flicker light-induced vasodilatation in the human retina: effect of lactate and changes in mean arterial pressure. *Invest Ophthalmol Vis Sci* 2003;44:5309-5314.

104. Garhofer G, Huemer KH, Zawinka C, Schmetterer L, Dorner GT. Influence of diffuse luminance flicker on choroidal and optic nerve head blood flow. *Curr Eye Res* 2002;24:109-113.

105. Michelson G, Patzelt A, Harazny J. Flickering light increases retinal blood flow. *Retina-the Journal of Retinal and Vitreous Diseases* 2002;22:336-343.

106. Riva CE, Logean E, Falsini B. Temporal dynamics and magnitude of the blood flow response at the optic disk in normal subjects during functional retinal flicker-stimulation. *Neuroscience letters* 2004;356:75-78.

107. Chatters T. An investigation of the light-induced changes in oxygen consumption in the outer retina of cat. *Bioengineering*: Northwestern University; 1988.

108. Linsenmeier RA. Effects of light and darkness on oxygen distribution and consumption in the cat retina. *J Gen Physiol* 1986;88:521-542.

109. Mandeville JB, Marota JJ, Ayata C, et al. Evidence of a cerebrovascular postarteriole windkessel with delayed compliance. *Journal of cerebral blood flow and metabolism : official journal of the International Society of Cerebral Blood Flow and Metabolism* 1999;19:679-689.

110. Shahidi M, Wanek J, Gaynes B, Wu T. Quantitative assessment of conjunctival microvascular circulation of the human eye. *Microvasc Res* 2010;79:109-113.

111. Cheung AT, Ramanujam S, Greer DA, Kumagai LF, Aoki TT. Microvascular abnormalities in the bulbar conjunctiva of patients with type 2 diabetes mellitus. *Endocr Pract* 2001;7:358-363.

112. Cheung AT, Tomic MM, Chen PC, Miguelino E, Li CS, Devaraj S. Correlation of microvascular abnormalities and endothelial dysfunction in Type-1 Diabetes Mellitus (T1DM): a real-time intravital microscopy study. *Clin Hemorheol Microcirc* 2009;42:285-295.

113. Smith MM, Chen PC, Li CS, Ramanujam S, Cheung AT. Whole blood viscosity and microvascular abnormalities in Alzheimer's Disease. *Clin Hemorheol Microcirc* 2009;41:229-239.

114. Wanek J, Gaynes B, Lim JI, Molokie R, Shahidi M. Human bulbar conjunctival hemodynamics in hemoglobin SS and SC disease. *Am J Hematol* 2013;88:661-664.

115. Kord Valeshabad A, Wanek J, Zelkha R, et al. Conjunctival microvascular haemodynamics in sickle cell retinopathy. *Acta Ophthalmol* 2014.

116. Paton D. The conjunctival sign of sickle-cell disease. *Arch Ophthalmol* 1961;66:90-94.

117. Jiang H, Ye Y, DeBuc DC, et al. Human conjunctival microvasculature assessed with a retinal function imager (RFI). *Microvasc Res* 2013;85:134-137.

118. Duench S, Simpson T, Jones LW, Flanagan JG, Fonn D. Assessment of variation in bulbar conjunctival redness, temperature, and blood flow. *Optometry and Vision Science* 2007;84:511-516.

119. van Zijderveld R, Ince C, Schlingemann RO. Orthogonal polarization spectral imaging of conjunctival microcirculation. *Graefes Arch Clin Exp Ophthalmol* 2014;252:773-779.

120. Koutsiaris AG, Tachmitzi SV, Papavasileiou P, et al. Blood velocity pulse quantification in the human conjunctival pre-capillary arterioles. *Microvasc Res* 2010;80:202-208.

121. Koutsiaris AG, Tachmitzi SV, Batis N. Wall shear stress quantification in the human conjunctival pre-capillary arterioles in vivo. *Microvasc Res* 2013;85:34-39.

122. Cheung AT, Perez RV, Chen PC. Improvements in diabetic microangiopathy after successful simultaneous pancreas-kidney transplantation: a computer-assisted intravital microscopy study on the conjunctival microcirculation. *Transplantation* 1999;68:927-932.

123. Burns SA, Tumbar R, Elsner AE, Ferguson D, Hammer DX. Large-field-of-view, modular, stabilized, adaptive-optics-based scanning laser ophthalmoscope. *Journal of the Optical Society of America a-Optics Image Science and Vision* 2007;24:1313-1326.

124. Hammer DX, Ferguson RD, Bigelow CE, Iftimia NV, Ustun TE, Burns SA. Adaptive optics scanning laser ophthalmoscope for stabilized retinal imaging. *Optics Express* 2006;14:3354-3367.

125. Hammer DX, Ferguson RD, Iftimia NV, et al. Advanced scanning methods with tracking optical coherence tomography. *Optics Express* 2005;13:7937-7947.

126. Nakagomi H, Hoshino K. Measurement of rotational eye movement using conjunctiva blood vessel tracking. *System Integration (SII), 2012 IEEE/SICE International Symposium on*; 2012:758-763.

127. Bradski G. The OpenCV library. *Dr Dobbs Journal* 2000;25:120-+.

128. Cherici C, Kuang X, Poletti M, Rucci M. Precision of sustained fixation in trained and untrained observers. *J Vis* 2012;12.

129. Yang Q, Bucci MP, Kapoula Z. The latency of saccades, vergence, and combined eye movements in children and in adults. *Invest Ophthalmol Vis Sci* 2002;43:2939-2949.

130. Wanek J, Blair NP, Shahidi M. Outer retinal oxygen consumption of rat by phosphorescence lifetime imaging. *Curr Eye Res* 2012;37:132-137.

131. Delaey C, Van De Voorde J. Regulatory mechanisms in the retinal and choroidal circulation. *Ophthalmic Res* 2000;32:249-256.

132. Linsenmeier RA, Braun RD, McRipley MA, et al. Retinal hypoxia in long-term diabetic cats. *Invest Ophthalmol Vis Sci* 1998;39:1647-1657.

133. Yu DY, Cringle SJ, Alder VA, Su EN. Intraretinal oxygen distribution in rats as a function of systemic blood pressure. *Am J Physiol* 1994;267:H2498-2507.

134. Petropoulos IK, Pournaras JA, Stangos AN, Pournaras CJ. Preretinal partial pressure of oxygen gradients before and after experimental pars plana vitrectomy. *Retina* 2013;33:170-178.

135. Yu DY, Cringle SJ, Alder VA. The response of rat vitreal oxygen tension to stepwise increases in inspired percentage oxygen. *Investigative ophthalmology & visual science* 1990;31:2493-2499.

136. Alder VA, Yu DY, Cringle SJ, Su EN. Changes in vitreal oxygen tension distribution in the streptozotocin diabetic rat. *Diabetologia* 1991;34:469-476.

137. Pournaras CJ, Tsacopoulos M, Riva CE, Roth A. Diffusion of O2 in normal and ischemic retinas of anesthetized miniature pigs in normoxia and hyperoxia. *Graefes Arch Clin Exp Ophthalmol* 1990;228:138-142.

CONTRIBUTION OF AUTHORS

The work presented in this thesis has, at least in part, been used to publish the following manuscripts in peer-reviewed journals, with specific author contributions provided:

- Anthony E. Felder, Justin Wanek, Norman P. Blair, Mahnaz Shahidi; Inner Retinal Oxygen Extraction Fraction in Response to Light Flicker Stimulation in Humans. Invest. Ophthalmol. Vis. Sci. 2015;56(11):6633-6637. doi: 10.1167/iovs.15-17321.

  AE Felder: study design, data acquisition, data processing, interpretation and writing
  J Wanek: data acquisition, interpretation and writing
  N P Blair: interpretation and writing
  M Shahidi: study design, data processing, interpretation and writing

- Anthony E. Felder, Justin Wanek, Norman P. Blair, Charlotte E. Joslin, Katherine C. Brewer, Felix Y. Chau, Jennifer I. Lim, Yannek I. Leiderman, Mahnaz Shahidi; The Effects of Diabetic Retinopathy Stage and Light Flicker on Inner Retinal Oxygen Extraction Fraction. Invest. Ophthalmol. Vis. Sci. 2016;57(13):5586-5592. doi: 10.1167/iovs.16-20048.

  AE Felder: study design, data acquisition, data processing, interpretation and writing
  J Wanek: data acquisition, interpretation and writing
  NP Blair: interpretation and writing
  CE Joslin: data processing and interpretation
  KC Brewer: data processing and interpretation
  FY Chau: data acquisition
  JI Lim: data acquisition
  YI Leiderman: data acquisition
  M Shahidi: study design, data processing, interpretation and writing

- Anthony E. Felder, Cesare Mercurio, Justin Wanek, Rashid Ansari, Mahnaz Shahidi; Automated Real-Time Conjunctival Microvasculature Image Stabilization. IEEE Trans. Med. Imaging 2016; 35(7):1670-1675. doi: 10.1109/TMI.2016.2522918

AE Felder: study design, data acquisition, data processing, interpretation and writing
C Mercurio: study design and data acquisition. N.B.: preliminary data from this study was used for a Master's Thesis (CM)
J Wanek: interpretation and writing
R Ansari: interpretation
M Shahidi: study design, data processing, interpretation and writing

The following articles have been submitted and are under peer review at the time of this thesis, with specific author contributions provided:

- Anthony E. Felder, Justin Wanek, Norman P. Blair, Mahnaz Shahidi; Retinal vascular and oxygen temporal dynamic responses to light flicker in humans. Invest. Ophthalmol. Vis. Sci. 2017.

  AE Felder: study design, data acquisition, data processing, interpretation and writing
  J Wanek: data processing
  NP Blair: interpretation and writing
  M Shahidi: study design, data processing, interpretation and writing

- Anthony E. Felder, Justin Wanek, Pang-yu Teng, Norman P. Blair, Mahnaz Shahidi; A Method for Volumetric Retinal Tissue Oxygen Tension Imaging. Curr. Eye Res. 2017

  AE Felder: study design, data acquisition, data processing, interpretation and writing
  J Wanek: data acquisition, data processing, interpretation and writing
  P Teng: data acquisition, data processing
  NP Blair: interpretation
  M Shahidi: study design, data processing, interpretation and writing

STATEMENT OF FUNDING

The work in this thesis was supported by NIH Grants DK010439, EY017918, and EY001792; Research to Prevent Blindness Awards: Senior Scientific Investigator Award (M. Shahidi), and an unrestricted departmental Award (UIC Ophthalmology & Visual Sciences).

APPENDIX

Approval for use of published data from IOVS (Felder 2015, Felder 2016) and IEEE TMI (Felder 2016) are included below.

Kiah Culver <kculver@arvo.org> Thu, Jan 26, 2017 at 8:51 AM
To: "afelde2@uic.edu" <afelde2@uic.edu>

Hello Dr. Felder,

I'm following up to your phone request yesterday concerning ARVO's copyright policy. The Journals team confirmed authors own the copyright to their published research. If such research will be reproduced in another publication, the author must obtain permission from ARVO, as the publication license holder.

Should you have further questions, you may contact a Journals team member at: iovs@arvo.org.

Kind regards,

Kiah

Kiah Culver

Senior Manager, Customer Service

Association for Research in Vision and Ophthalmology
1801 Rockville Pike, Suite 400, Rockville, MD 20852, U.S.A.
Direct: +1.240.221.2945 | Main: +1.240.221.2900
kculver@arvo.org
www.arvo.org

Copyright Clearance Center RightsLink® Home Create Account Help

IEEE Requesting permission to reuse content from an IEEE publication

Title: Automated Real-Time Conjunctival Microvasculature Image Stabilization
Author: Anthony E. Felder
Publication: Medical Imaging, IEEE Transactions on
Publisher: IEEE
Date: July 2016

LOGIN
If you're a copyright.com user, you can login to RightsLink using your copyright.com credentials. Already a RightsLink user or want to learn more?

Thesis / Dissertation Reuse

The IEEE does not require individuals working on a thesis to obtain a formal reuse license, however, you may print out this statement to be used as a permission grant:

Requirements to be followed when using any portion (e.g., figure, graph, table, or textual material) of an IEEE copyrighted paper in a thesis:

1) In the case of textual material (e.g., using short quotes or referring to the work within these papers) users must give full credit to the original source (author, paper, publication) followed by the IEEE copyright line © 2011 IEEE.
2) In the case of illustrations or tabular material, we require that the copyright line © [Year of original publication] IEEE appear prominently with each reprinted figure and/or table.
3) If a substantial portion of the original paper is to be used, and if you are not the senior author, also obtain the senior author's approval.

Requirements to be followed when using an entire IEEE copyrighted paper in a thesis:

1) The following IEEE copyright/ credit notice should be placed prominently in the references: © [year of original publication] IEEE. Reprinted, with permission, from [author names, paper title, IEEE publication title, and month/year of publication]
2) Only the accepted version of an IEEE copyrighted paper can be used when posting the paper or your thesis on-line.
3) In placing the thesis on the author's university website, please display the following message in a prominent place on the website: In reference to IEEE copyrighted material which is used with permission in this thesis, the IEEE does not endorse any of [university/educational entity's name goes here]'s products or services. Internal or personal use of this material is permitted. If interested in reprinting/republishing IEEE copyrighted material for advertising or promotional purposes or for creating new collective works for resale or redistribution, please go to http://www.ieee.org/publications_standards/publications/rights/rights_link.html to learn how to obtain a License from RightsLink.

VITA

Name: Anthony E. Felder

Education:

2017: **University of Illinois at Chicago, Chicago, IL**
College of Engineering, Department of Bioengineering
Doctorate of Philosophy in Bioengineering

2011: **University of Illinois at Chicago, Chicago, IL**
College of Engineering, Department of Bioengineering
Bachelor of Science in Bioengineering / Minor in Mathematics

Honors:

2015: **University of Illinois at Chicago, Chicago, IL**
College of Medicine PECTS Scholarship

2013: **University of Illinois at Chicago, Chicago, IL**
Graduate Student Travel Grant

2011: **University of Illinois at Chicago, Chicago, IL**
Bell Honor Award

Publications:

2017: **Felder, A. E.**, et al. (2017). Retinal Vascular and Oxygen Temporal Dynamic Responses to Light Flicker in Humans. Investigative Ophthalmology & Visual Science. (Submitted – R0).

2017: **Felder, A. E.**, et al. (2017). A Method for Combined Retinal Vascular and Tissue Oxygen Tension Imaging. Scientific Reports. (Submitted – R0).

2017: **Felder, A. E.**, et al. (2017). A Method for Volumetric Retinal Tissue Oxygen Tension Imaging. Current Eye Research. (Submitted – R1).

2017: Blair, N.P., et al. (2017). Retinal Oximetry and Vessel Diameter Measurements with a Commercially Available Scanning Laser Ophthalmoscope in Diabetic Retinopathy. Investigative Ophthalmology & Visual Science. (Submitted – R1).

2016: Blair, N. P., et al. (2016). "Inner Retinal Oxygen Delivery, Metabolism and Extraction Fraction in $Ins2^{Akita}$ Diabetic Mice." Investigative Ophthalmology & Visual Science.

2016: **Felder, A. E.** et al. (2016). "The Effects of Diabetic Retinopathy Stage and Light Flicker on Inner Retinal Oxygen Extraction Fraction." Investigative Ophthalmology & Visual Science.

2016: **Felder, A.**, et al. (2016). "Automated Real-time Conjunctival Microvasculature Image Stabilization." IEEE Transactions on Medical Imaging.

2015: Khansari, M. M., et al. (2015). "Automated assessment of hemodynamics in the conjunctival microvasculature network." IEEE Transactions on Medical Imaging.

2015: **Felder, A. E.**, et al. (2015). "Inner Retinal Oxygen Extraction Fraction in Response to Light Flicker Stimulation in Humans." Investigative Ophthalmology & Visual Science.

Presentations:

05/17: **Association for Research in Vision and Ophthalmology, Baltimore, MA**
Quantitative Volumetric Analysis of Retinal Tissue Oxygen Tension

05/17: **Association for Research in Vision and Ophthalmology, Baltimore, MA**
Alterations in Retinal Oxygen Delivery and Metabolism due to Experimental Retinal Ischemia

05/17: **Association for Research in Vision and Ophthalmology, Baltimore, MA**
A Rodent Model of Graded Reduction of Retinal Blood Flow for Ischemia Research

05/17: **Association for Research in Vision and Ophthalmology, Baltimore, MA**
A Method for Combined Retinal Vascular and Tissue Oxygen Tension Imaging

03/17: **International Society for Magnetic Resonance in Medicine, Honolulu, HI**
Phosphorescence Lifetime Imaging to validate BOLD MRI Derived blood PO_2

05/16: **Association for Research in Vision and Ophthalmology, Seattle, WA**
Temporal Dynamics of Inner Retinal Vasculature and Oxygen Extraction Fraction during Light Flicker Stimulation in Humans

05/16: **Association for Research in Vision and Ophthalmology, Seattle, WA**
Inner Retinal Oxygen Delivery and Metabolism Following Ischemia/Reperfusion Injury in Rat

05/16: **Association for Research in Vision and Ophthalmology, Seattle, WA**
Alterations in Retinal Tissue Oxygen Tension due to Light Flicker Stimulation in Rat

05/15: **Association for Research in Vision and Ophthalmology, Denver, CO**
A Method for Simultaneous Assessment of Retinal Vascular oxygenation and Diameter in Response to Light Flicker in Humans

05/15 **Association for Research in Vision and Ophthalmology, Denver, CO**
Inner Retinal Oxygen Delivery and Metabolism in Diabetic Mice

09/14: **Association for Ocular Circulation, Chicago, IL**
Retinal Oximetry and Vascular Response to Light Flicker in Rats

02/14: **American Association for the Advancement of Science, Chicago, IL**
Development and Application of an Ultrafast Laser Microsurgery Platform to Remove Cilia

11/13: **University of Illinois at Chicago College of Medicine Research Forum, Chicago, IL**
Development of an ultrafast laser microsurgery platform with application in primary and ependymal cilia removal

09/13: **Biomedical Engineering Society, Seattle, WA**
Development and application of an ultrafast laser microsurgery platform to precisely remove cilia

05/13: **Biomedical Engineering Society, Chicago, IL**
Development and application of an ultrafast laser microsurgery platform to perform precise cilium removal

11/12: **University of Illinois at Chicago College of Medicine Research Forum, Chicago, IL**
Acute neuronal cilia ablation by ultrafast laser microsurgery